Seismic ambient noise analyses reveal changing temperature and water signals to 10s of meters depth in the critical zone

David O. S. Oakley[1,†], Brandon Forsythe[1], Xin Gu[1,2], Andrew A. Nyblade[2], Susan L. Brantley[1,2]

[1]Earth and Environmental Systems Institute, Pennsylvania State University, University Park, PA 16802

[2]Department of Geosciences, Pennsylvania State University, University Park, PA 16802

[†]Now at Department of Energy Resources, University of Stavanger, 4036 Stavanger, Norway

Corresponding author: David Oakley (david.o.oakley@uis.no)

Key Points

- We use high-frequency ambient seismic noise to detect changes in seismic velocity in the critical zone at the Shale Hills catchment.
- We observe diurnal, meteorological-event-based, and seasonal changes in velocity.
- We interpret velocity changes to be primarily driven by temperature changes at the surface, while water movement plays a secondary role.

Abstract

The critical zone sustains terrestrial life, but we have few tools to explore it efficiently beyond the first few meters of the subsurface. Using analyses of high-frequency ambient seismic noise from densely-spaced seismometers deployed in the forested Shale Hills subcatchment of the Susquehanna Shale Hills Critical Zone Observatory (SSHCZO), we show that temporal changes in seismic velocities at depths from ~1 m to 10s of m can be detected. These changes are driven by variations at the land surface. The Moving-Window Cross-Spectral (MWCS) method was employed to measure seismic-velocity changes in coda waves at hourly resolution in ten different frequency bands. We observed a diurnal signal, a seasonal signal, and a meteorological-event-based signal. These signals were compared to time-series measurements of precipitation, well water levels, soil moisture, soil temperature, air temperature, latent heat flux, and air pressure in the heavily instrumented catchment. Most of the velocity changes can be explained by variations in temperature that result in thermoelastic strains that propagate to depth. But some double minima in seismic velocity time-series observed after large rain events were attributed in part to the effects of water infiltration. These results show that high-frequency ambient noise data may in some locations be used to detect changes in the critical zone from ~1 m to ~100 m or greater depth with hourly resolution. But interpretation of such data requires multiple environmental datasets to deconvolve the complex inter-relationships among thermoelastic and hydrological effects in the subsurface critical zone.

Plain Language Summary

Measuring changes in Earth's subsurface over time is necessary to understand processes such as groundwater flow and soil formation that are important to human life, but unlike at the Earth's surface, these underground changes are difficult to observe directly. In this study, we analyzed vibrations in the ground driven by ambient noise at the land surface. By measuring small changes in the velocity of seismic waves moving through the earth, we detected changes occurring in the upper ~100 m over several months. We observed seismic-velocity changes related to daily and longer-term seasonal weather variations. We were able to interpret the data because we compared our results to a multitude of environmental measurements at the same location. We attribute most of the changes in seismic velocity to changes in temperature at the surface that in turn create small stresses in the earth that propagate downward. We also observed velocity changes after rainstorms that are likely caused by the infiltration of water into the ground.

1. Introduction

1.1 Ambient Noise

Time-varying environmental processes within Earth's critical zone, such as water movement and temperature changes, are essential in making it a habitable environment for life and in driving processes such as bedrock weathering and soil formation. These processes can be readily observed in the above-ground parts of the critical zone – defined as the region in which rock, soil, air, water, and life interact (Brantley et al., 2007) – but below ground, they can only be directly observed by drilling. This limits direct observations to a few narrow and widely spaced locations. Geophysical methods provide an alternative way to observe the subsurface critical zone without the need for drilling (Holbrook et al., 2014; Parsekian et al., 2015), but most geophysical methods provide only a snapshot in time. In this study, we use ambient-noise seismology to observe subsurface changes in seismic velocity within the critical zone of the heavily instrumented Shale Hills watershed in central Pennsylvania. Together with the extensive set of ancillary data recorded at the surface in the watershed, these observations provide insight into how changes at the land surface propagate downward to deeper within the critical zone and show that high-frequency (10s–100s of Hz) ambient noise can reveal changes in the critical zone at sub-daily temporal resolution.

Ambient-noise seismology is a relatively new geophysical technique based on the cross-correlation of ambient vibrations recorded at two different seismometers. It differs from more traditional methods that require an active energy source such as a hammer blow and so are less suited to continuous monitoring. Application of ambient-noise seismology to critical zone studies is in its early stages (Parsekian et al., 2015), but the method holds significant promise. Because ambient noise can be passively recorded over long periods of time, ambient-noise seismology is well suited to detecting temporal changes in seismic velocity and therefore to studying time-varying critical zone processes. While ambient- noise seismology has been previously applied to image the near surface, especially in engineering applications (e.g. Planès et al., 2016; Joubert et al., 2018), it has only occasionally been used to study time-varying critical zone processes (e.g. in the permafrost studies of James et al., 2017; 2019). Further, high-frequency time-lapse ambient noise studies have been limited to frequencies below 40 Hz, and still higher- frequency ambient noise offers the possibility to distinguish changes occurring within the top few meters of the critical zone.

Ambient-noise seismology makes use of background seismic vibrations, produced by both natural processes and human activity, rather than distinct events such as earthquakes or the energy from active seismic sources. Cross-correlation of the ambient wavefield at two different seismometers over sufficiently long periods of time can be used to approximate the Green's function between the two sensors (Sabra, Gerstoft, Roux, Kuperman, and Fehler, 2005; Shapiro and Campillo, 2004). The technique was initially applied to crustal-scale studies (Sabra, Gerstoft, Roux, and Kuperman, 2005; Shapiro et al., 2005), but more recent work has applied it to imaging of the shallow subsurface (e.g. Picozzi et al., 2009; Pilz et al., 2012; 2013; 2014) and even to critical-zone studies (e.g. Kiefer et al., 2019; Wang et al., 2019) using high-frequency ambient noise (up to 130 Hz in Kiefer et al., 2019). These and most other ambient-noise studies make use of Rayleigh waves, which are typically the dominant wave type observed in ambient-noise cross-correlations. Rayleigh waves are most sensitive to seismic velocity (especially Vs) at a depth that depends on frequency, with higher frequencies being more sensitive to shallower depths. The most significant noise sources at frequencies higher than 1 Hz are typically anthropogenic (Bonnefoy-Claudet et al. 2006), such as from road traffic, and we expect that the same is true at the SSHCZO, which is adjacent to a road, although natural sources of noise such as wind may also play a role. An analysis of noise sources is, however, beyond the scope of this study.

Beginning with Sens-Schönfelder and Wegler (2006), ambient noise has been used not only for static imaging but also for measuring changes in velocity over time by detecting small changes in travel time within the coda of the cross-correlation. While many of these studies have again focused on depths much greater than those relevant to the critical zone, ambient noise at high frequencies ranging from 1.5 to 39 Hz has been used to detect changes in seismic velocity in the shallow subsurface in engineering applications (e.g. Planès et al., 2016; Joubert et al., 2018) and in the study of landslides (Voisin et al., 2016), permafrost (James et al. 2017; 2019), ground freezing (Gassenmeier et al., 2015), and rock glaciers (Guillemot et al., 2020). While previous critical-zone geophysical studies have mostly focused on changes in space, this approach provides the potential for studying changes in time. To our knowledge, the highest frequency targeted for previous applications of ambient noise to study velocity changes is that of Joubert et al. (2018), who used a 21–39 Hz frequency band to observe changes in a sea dike. Our study, which considers frequency bands as high as 100–200 Hz thus aims to apply this technique at higher frequencies (and thus shallower depths) than previously studied, in order to better observe very near surface critical-zone processes.

A variety of physical processes can drive seismic-velocity changes, with hydrological and meteorological processes being of most interest for critical-zone studies. Increases in the water saturation of soil or rock driven by infiltration after a rainstorm are expected to increase P-wave velocity (Vp) and decrease S-wave velocity (Vs). For the type of study we are conducting, this change typically results in a net decrease in the observed velocity due to the ambient noise being dominated by surface waves (Clements and Denolle, 2018; Kim and Lekic, 2019). Such effects have been observed in other recent studies of ambient seismic noise (e.g. Civilini et al., 2020; Clements and Denolle, 2018; Fores et al., 2018; Hillers et al., 2014; Joubert et al., 2018; Kim and Lekic, 2019; Lecocq et al., 2017; Liu et al., 2018; Rivet et al., 2015; Sens-Schönfelder and Wegler, 2006; Viens et al., 2018; Viens and Van Houtte, 2020; Voisin et al., 2016; Wang et al., 2017), but our work extends the analysis to higher frequencies and allows comparison with other types of environmental data. Temperature changes at the surface are also known to drive seismic-velocity changes at depth, as has been observed in a number of previous ambient-noise studies, again mostly working at lower frequencies, including those by Hillers et al. (2015), Hillers et al. (2019), Lecocq et al. (2017), Mao et al. (2019), Meier et al. (2010), Qui et al. (2020), and Richter et al. (2014). As temperature increases, velocity is expected to increase due to thermoelastic stresses (Richter et al., 2014). Finally, at least one team (Olivier and Brenguier, 2016) has also observed long-term seismic-velocity changes due to air-pressure changes (with velocity increasing as air pressure increases), although those changes were almost undetectably small (about 0.002%). Besides these hydrological and meteorological processes, other processes that may drive changes in seismic velocity include tides (Takano et al., 2014; Mao et al., 2019), earthquakes (Wegler and Sens-Schönfelder, 2007; Brenguier, Campillo, et al., 2008), and volcanic activity (Brenguier, Shapiro, et al., 2008).

1.2 Shale Hills

Our study was conducted at the Shale Hills catchment of the Susquehanna / Shale Hills Critical Zone Observatory (SSHCZO) in central Pennsylvania, U.S.A. (Figure 1). The inland, tectonically quiet location is well suited for observing changes in seismic velocity related to temperature changes and water movement in the critical zone. Shale Hills is a first-order catchment developed on Silurian Rose Hill shale. As a Critical Zone Observatory, it is a heavily instrumented and intensively studied watershed, which provides an ideal location to relate changes detected by our ambient-noise experiment to critical-zone processes that are continuously monitored by the variety of hydrological and meteorological instruments at the site. Previously, the temporal dynamics of moisture storage and preferential flow in soil (Lin, 2006; Guo et al., 2014) have been studied at Shale Hills, but the dynamics of the deeper critical zone have not been studied.

Within the SSHCZO, we focus on the South Planar Transect, a well-studied hillslope on the south side of the catchment. The South Planar Transect has been the focus of previous studies, beginning with Jin et al. (2010), and contains multiple instrument sites at ridge top (SPRT), mid-slope (SPMS), and valley floor (SPVF) locations. We focus on the SPMS and SPVF sites, allowing us to observe seismic-velocity variations at two sites with different water table depths and potentially different responses to hydrologic or other events.

2. Data and Methods

2.1 Data

For ambient-noise data collection, we used 5 Hz three-component Magseis FairfieldNodal ZLand seismometers borrowed from IRIS PASSCAL. The seismometers were set to a sampling frequency of 1000 Hz, allowing us to measure ambient noise at frequencies up to 500 Hz (the Nyquist frequency). To interrogate processes in different seasons, the seismometers were deployed from March 20 to June 11, 2019 and again from October 2 to 29, 2019. Since the seismometer batteries last for about a month, the nodes in the spring deployment were replaced with fresh ones on April 22 and May 22. While 50 seismometers were deployed in the experiment, in this paper we primarily use data from two dense subarrays, each consisting of nine seismometers spaced about 5 m apart, that were deployed at the SPMS and SPVF instrumentation sites (red triangles in Figure 1). Data from some additional seismometers (orange triangles in Figure 1) were used only in constructing a 1D velocity model. The data are archived at the IRIS data management center using the network codes XZ and 5A (Nyblade, 2019a, 2019b).

Data on hydrological and meteorological processes occurring in the CZO came from the large number of continuously operating instruments in this watershed (Brantley et al., 2016, 2018). GroundHOG sites (Brantley et al., 2016; Tang et al., 2020) recorded soil moisture and soil temperature separately at SPMS and SPVF and precipitation at SPMS (Li and Eissenstat, 2020a, 2020b; Eissenstat et al., 2020). Water levels were monitored in three wells near the SPMS and SPVF sites (CZMW8 at the ridge crest and Wells 5 and 7 at the valley floor) (Brantley and Gu, 2020a, 2020b, 2020c). Barometric pressure and air temperature were also measured at CZMW8

(Brantley and Gu, 2020d). Latent heat flux, which provides a measure of evapotranspiration, was measured at the flux tower on the northern side of the watershed, approximately 258 m from SPMS (Davis, 2020). Locations of all these instruments are shown in Figure 1. For this study, measurements from these instruments were averaged or summed as appropriate over hour-long time segments to compare to the hourly time scale on which we observed seismic-velocity changes.

2.2 Ambient Noise Cross-Correlation

Ambient-noise data were processed with the MSNoise version 1.6 software (Lecocq et al., 2014), mostly following the steps described by Bensen et al. (2007). Raw three-component seismograms were cut into hour-long segments and high-pass filtered above 5 Hz, and instrument responses were removed. The three component seismograms were then rotated into a coordinate system aligned with the local surface slope. (To do this, we slightly modified the original MSNoise code.) We approximated the surface as locally planar at each of the subarrays, using the best-fit plane to the nine station locations in each subarray; these define a slope of 23.13° with aspect 8.89° at SPMS and a slope of 9.49° with aspect 351.67° at SPVF. This rotation was done because high-frequency surface waves are expected to follow topography (Ping et al., 2020). For each pair of stations, the horizontal components were further rotated into radial and transverse directions within the slope-aligned coordinate system prior to cross-correlation.

After rotation, hourly seismograms were split into 20-second-long, 75%-overlapping segments (Seats et al., 2012), which were spectrally whitened and clipped at 3 times RMS amplitude. For each time segment, the data were then cross-correlated between all possible station pairs (36 pairs for 9 stations in each subarray), and the cross-correlations were trimmed to a maximum lag time of 3 seconds. The cross-correlations for each station pair were then stacked for each hour of each day during the study period. Cross-correlations were computed for the vertical (Z) and radial (R) components of ground motion (ZZ and RR cross-correlations), where vertical is defined as perpendicular to the local slope and radial is parallel to the slope.

2.3 Moving-Window Cross-Spectral Analysis

To measure changes in seismic velocity over time, we used the Moving-Window Cross-Spectral (MWCS) technique (Clarke et al., 2011; Poupinet et al., 1984) on the vertical component cross-correlations. MWCS operates on the coda of cross-correlations (Figure 2), which is more stable over time than is the direct surface wave (Colombi et al., 2014), and it detects small changes in velocity relative to a reference cross-correlation. The cross-correlations were filtered within a frequency band of interest, a sliding window was used to select short segments in time within the coda, and the phase of the cross spectrum between each waveform and the reference as a function of frequency was used to calculate a change in travel time (dt). A linear regression was then performed over all dt vs. t (the center time of the sliding window) pairs, and the change in velocity (dv) relative to the reference velocity (v) was calculated as

$$\frac{dv}{v} = -\frac{dt}{t} \qquad (1)$$

In this study, we used MWCS to detect changes in velocity on an hourly time scale, using a stack over the entire spring deployment (March 20 to June 11) as the reference waveform. We used the singular-value-decomposition-based Wiener filter (SVDWF) of Moreau et al. (2017) to reduce noise in the data prior to MWCS. We kept singular values equal to 95% of the total sum of all singular values, and we used a filter order of 5 in both dimensions of the Wiener filter (hour and cross-correlation lag time). We did SVDWF filtering after bandpass filtering in each frequency band and after windowing the coda waves (separately on the causal and acausal sides) in order to focus on the part of interest for this study.

We conducted MWCS analysis within ten overlapping frequency bands, in which the maximum frequency was twice the minimum frequency: 5–10, 10–20, 15–30, 20–40, 30–60, 40–80, 50–100, 60–120, 80–160, and 100–200 Hz. The MWCS window length was three times the longest period (T_{max}) in each MWCS frequency band, and the window was moved with a step size of half T_{max}. The lag times used for MWCS depended on interstation distance (d) and the longest period in each MWCS frequency band. Assuming a minimum direct-wave velocity (v_{min}) of 100 m/s (a conservative estimate – see Figure 3a and b), the part of the coda used for the analysis began at $d/v_{min} + 2/T_{max}$ and had a width of 10 T_{max} (Figure 2).

In order to increase the signal-to-noise ratio and to avoid the possibility that changes in the noise source distribution could affect the observed dv/v (Colombi et al., 2014), we used the dt vs. t values from all thirty-six station pairs in each subarray to calculate a single dv/v for each of the two sites. We fit a line to the dt vs. t data, forcing it to go through the origin, and calculated dv/v from its slope and Eqn. 1. In this regression, dt values were used only if they met three conditions: the coherence between the hourly and reference waveforms was ≥ 0.80, the error in the dt value was ≤ 0.01, and the dt/t value was ≤ 0.02. These conditions removed outliers and restricted the analysis to times at which the hourly waveform could be clearly interpreted as a phase-shifted version of the reference waveform.

The MWCS procedure requires a number of user-chosen parameters, as listed above. There are not yet established standards for these values, but our choices are generally similar to previous work (except in using high frequencies). We describe the reasons for our choices further in Text S1. The only choice that we found to have a substantial effect on the results was the width of the coda window (Text S1 and Figure S1), which affects the amplitudes of the dv/v variations that we observe.

2.4 Group Velocity Measurement and Velocity Model

In order to estimate the depths at which velocity changes revealed by MWCS occurred, we must have a velocity model from which to calculate sensitivity of Rayleigh waves to changes in shear wave velocity (V_S) as a function of depth. For this, we used frequency-time analysis (FTAN) (Dziewonski et al., 1969; Levshin and Ritzwoller, 2001) to find a Rayleigh-wave group-velocity dispersion curve centered on SPMS, which we then inverted for a one-dimensional shear-wave velocity model. In FTAN analysis, cross-correlations are filtered with Gaussian filters to produce a frequency-time diagram, which is interpolated to frequency-velocity based on the interstation distance, and the group-velocity dispersion curve is picked along a maximum amplitude ridge of the diagram. Our FTAN analysis was based on the methods described in Bensen et al. (2007), with some modifications.

For FTAN analysis, we used cross-correlations stacked over the entire spring deployment in order to produce an average velocity model. We made use of not only the 36 station pairs within the SPMS subarray, but also of longer offset pairs within a set of 10 additional stations around it (orange triangles in Figure 1), which are approximately (within 0.5 m) on the same topographic plane as the SPMS stations and could therefore be rotated into the same slope-aligned coordinate system. In total, we considered a range of interstation distances from 4.6 to 57.6 m. Cross-correlations with similar interstation distances (binned in 0.25 m increments) were stacked together to help increase signal-to-noise ratio (Boué et al., 2013; Mordret et al., 2014; 2020; Nakata et al., 2015). Cross-correlations were then high-pass filtered at the frequency that would produce a wavelength equal to the interstation distance – typically the limit for FTAN analysis (Luo et al., 2015) – at a velocity of 350 m/s (a value chosen empirically after initial analysis). The causal and acausal sides of each cross-correlation were then averaged. We conducted FTAN on the ZZ and RR cross-correlation components, since these (as well as the ZR and RZ components) record Rayleigh waves and can be used together to improve dispersion curve identification (Pan et al., 2018; Zigone et al., 2015). We did not use ZR and RZ because we found that these reduced the sharpness of the FTAN peak amplitude for our data. Dispersion images from all interstation distances and both components were individually normalized and then stacked together in the frequency-velocity domain to produce a single dispersion image. A preliminary dispersion curve was extracted from this dispersion image, and instantaneous frequencies for this curve (Bracewell, 1978) were calculated based on the amplitude-weighted average of instantaneous frequencies from the individual stacked dispersion diagrams. Finally, cross-correlations were windowed in time around the range of velocities in the preliminary dispersion curve, and this dispersion curve was used to perform phase-matched filtering (Levshin and Ritzwoller, 2001) on the cross-correlations to produce cleaned dispersion images, which were again stacked to produce the final dispersion images, from which the final dispersion curve was extracted.

To fit one-dimensional velocity models to the dispersion curve, we used the hierarchical, transdimensional Markov chain Monte Carlo method of Bodin et al. (2012). In this method, the number of layers in the model and the uncertainty in the data are not fixed but are determined from the data. The method produces an ensemble of models drawn from the posterior distribution of model parameters, which can be used to calculate both an average model and its uncertainty. Following Gao and Lekić (2018), we inverted for V_S and V_P/V_S with independent parameterization. Rayleigh waves are only weakly sensitive to Vp/Vs, but inverting for both avoids making a potentially-incorrect assumption about Vp/Vs and allows us to constrain it to the extent allowed by the data. Density was calculated using the equation of Gardner et al. (1974). Based on velocities in well logs from CZMW8 and 10 (Gu et al., 2020), the maximum Vs was limited to 2600 m/s. Low velocity zones were allowed but were limited to a 40% drop in velocity (again based on what is seen in the well logs) in order to avoid physically-unreasonable solutions and limit the non-uniqueness of results. The range of Vp/Vs as a function of Vs was limited to values allowed by the rock-physics model of Gu et al. (2020) for Shale Hills, in order to limit the non-uniqueness of inverting for both Vs and Vp/Vs. Forward modeling of dispersion curves from the layered models used a computer code from Herrmann et al. (2013). Further details of the choices made in the velocity inversion, are given in supporting Text S2.

Finally, we used the mean one-dimensional velocity model to calculate the sensitivity of Rayleigh-wave phase velocity to changes in V_S as a function of depth. Rayleigh-wave phase velocity is expected to be the primary control on the phase-shifts measured by MWCS under the assumption that ambient noise is dominated by surface waves, and Rayleigh-wave velocities are primarily controlled by V_S. To calculate sensitivity kernels, we used the relative difference method (Feng et al., 2001 as cited by Luo et al., 2011), in which we perturbed V_S slightly in each layer and recorded the percent change in Rayleigh-wave phase velocity.

3. Results

3.1 1D Velocity Model

Dispersion images (Figures 3a–b and S2) show a dispersion curve that is nearly flat at about 350 m/s at high frequencies and is almost vertical at low frequencies, with a sharp bend at about 20 Hz. Since only one curve is apparent, we assumed that it represents the fundamental mode. The final dispersion curve (Figure 3b) was sampled with logarithmic spacing at 25 points between 15 and 325 Hz, and these data were used for the velocity inversion. The resulting V_S model is shown in Figures 3c, the corresponding Vp, Vp/Vs and density models in Figure S3, and the fit of the mean model to the data in Figure S4. The model shows an abrupt increase in velocity between about 8 and 10 m depth. Since our model is parameterized in terms of discrete layers, it may overestimate the sharpness of the boundary to some degree, but our results clearly indicate a significant change in velocity at these depths. Below about 10 m, the Vs model agrees well with velocities from sonic logs of wells elsewhere in the SSHCZO (Figure 3c). Vs data for these wells are available only from below the well casing, so they cannot be compared to the upper 10 m of the velocity model.

To understand the physical origin of the velocity structure, we calculated porosity and water saturation from the velocity model using the rock-physics model of Gu et al. (2020) for Shale Hills (Figure 3d–e). The results show a large drop in porosity and increase in water saturation at about 8–10 m depth where Vs also changes abruptly, although water saturation is highly uncertain, likely due to the lower sensitivity of Rayleigh waves to Vp/Vs. Previous studies have identified a highly porous fractured bedrock layer that is no deeper than 10 m at the surface of the SSHCZO (Brantley et al., 2013; Jin et al., 2010; Jin, Rother, et al., 2011; West et al., 2019). West et al. (2019) have argued the layer is due to frost cracking during past periglacial climate conditions. In addition, Gu et al. (2020) have shown that porosity increases significantly above the depth where chlorite dissolves to react and create significant porosity in the shale matrix. The large increase in water saturation at about 8–10 m depth suggests that the water table also lies at about this depth. The transition that we see at 8–10 m may thus represent some combination of i) the base of the heavily-fractured layer, ii) the base of chlorite dissolution, and iii) the water table. In all three cases, the depths are reasonable. The fractured layer, as identified from P-wave refraction tomography by West et al. (2019), spans highly-variable depths of up to 10 m on north-facing hillslopes such as the South Planar Transect. The base of the chlorite-weathering zone lies at about 6 m depth in the valley at CZMW10 and 15 m depth at the ridge crest at CZMW8 (Gu et al., 2020), or about 10.5 m depth at mid-slope if linearly extrapolated (Figure 3). The water table averaged 1.25 m depth during our spring deployment in wells 5 and 7 near the valley floor (18 and 47 m away from SPVF respectively) and 17.7 m in well CZMW8 at the ridge crest (42 m distant from SPMS) (Figure 1), and geochemical evidence for groundwater at about 1 m depth at SPVF was reported previously by Jin, Andrews, et al. (2011). Again assuming a linear gradient, these depths put the estimated water table at 9.4 m depth at SPMS (Figure 3). Thus all three boundaries are plausible explanations for the changes that we see at 8–10 m depth and are likely too close together at SPMS to be distinguished in our velocity profile. Furthermore, these three phenomena are likely to be coupled to one another in this part of the watershed anyway.

The sensitivity curves for Rayleigh wave phase velocity (Figures 3f, S6–7) show that the frequency bands used in our MWCS analysis (Figures 4 and S8-9) are sensitive to a wide range of depths within the critical zone. Estimates of the depths of peak sensitivity for these bands are given in Table S1 and alongside the spectrograms in Figure 5. The highest-frequency band of 100–200 Hz has its peak sensitivity between 0.6 m and 1.4 m, while the lowest-frequency bands are sensitive to depths below 30 m. However, the peak sensitivity depths of the lower frequencies, and especially of 20 and 30 Hz, are significantly uncertain (see Text S3). The soil thickness is 0.6 m at SPMS and 0.7 m at SPVF (Jin et al., 2010), so even the highest-frequency band is unlikely to be very sensitive to processes occurring in the soil; instead we primarily expect to observe processes operating in the weathered rock (termed saprock by Jin, Rother, et al., 2011) or even deeper in the unweathered bedrock. Based on the sensitivity curves, we estimate that frequencies of 40 Hz and above are mostly sensitive to the vadose zone, 20 and 30 Hz are likely to be sensitive to depths spanning the water table and chlorite-weathering zone, and 15 Hz and below are mostly sensitive to depths below the water table and chlorite-weathering zone. This latter thus likely includes the depths of deeper weathering reactions such as pyrite oxidation or even bedrock that is entirely unweathered. Thus, our data span a large depth range within the critical zone with significant variation in porosity and saturation, including the depths necessary to observe processes operating in the vadose zone, fluctuations of the water table, and processes operating below the water table.

3.2 MWCS

The results of our MWCS analysis show velocity changes of < 1% occurring on multiple time scales (Figures 4 and S8–9), which exceed the level of uncertainty in the measurements (Figures S10–11). There is a strong diurnal signal at both SPMS and SPVF, which can be seen clearly in a spectral analysis of the dv/v time-series (Figure 5) and appears to some degree in all the frequency bands studied. There is also a much weaker semidiurnal signal, visible most clearly in the 15–30 Hz band, but not clearly identifiable in all frequency bands. To distinguish other signals from the diurnal variation, we apply a lowpass filter (at 0.8 cycles/day) to the data

(Figure 4) to highlight non-cyclical and long-term changes. These changes show a high degree of consistency between SPMS and SPVF (Figure 4).

Spectrograms of CZO datasets for soil moisture, soil temperature, well water levels, air temperature, air pressure, and latent heat flux (Figure 6) show non-cyclical and cyclical signals. Specifically, soil moisture and valley well water level spectrograms are dominated by the effects of short-term rain events (non-cyclical). Many of the rest show diurnal and often also semidiurnal signals. For example, well water levels show persistent diurnal and semidiurnal cycles, best visible in the ridge-top well CZMW 8 where the semidiurnal signal is especially strong. Air temperature shows a very strong diurnal signal as well as a fairly strong semidiurnal signal. Soil temperature shows the diurnal signal, decreasing in strength with depth, but the semidiurnal signal is much weaker and is not clearly seen at all at 40 cm depth. Air pressure shows a strong semidiurnal signal and a much weaker diurnal signal. Finally, latent heat flux shows clear diurnal and semidiurnal signals with the diurnal signal stronger. These latent heat flux signals increase markedly in strength in early May and have decreased again by October, likely reflecting the effect of leaf growth and death on evapotranspiration.

To further elucidate the relationship between dv/v and environmental datasets, we have filtered all datasets between 0.8 and 1.2 cycles/day to isolate the diurnal signal and then cross-correlated them. Figure 7 shows the maximum correlation coefficient and associated lag time for each dv/v frequency band compared to each environmental dataset. The lag time that is plotted is that of maximum positive correlation for the top two rows and maximum negative correlation for the bottom two, based on the expected physical relationships (i.e. dv/v should increase with increasing temperature and decrease with increasing subsurface water), and we consider only positive lags, indicating that the velocity change follows the environmental change as expected for a causal relationship. Due to the narrowband filtering, it is difficult to distinguish a positive lag from a negative one with a 24 hour difference (see Figure S15).

The strongest correlations are seen with air temperature, and water-related correlations (soil moisture and well water levels) are much weaker. Correlations with latent heat flux are similar to those with temperature, likely because temperature changes drive evapotranspiration changes. In the lowest four frequency bands, there is a lag time of several hours with air temperature, with progressively shorter lags for soil temperatures at 10 and 20 cm depths. (The long lag at 40 cm for some low-frequency data points shows weaker correlation and given the zero lag time for two of the data points may be a product of the 24 hour phase ambiguity.) The higher-frequency bands (30–60 Hz and up) show a near-zero lag with air temperature, indicating a rapid response to temperature changes. These frequencies show longer lags with soil temperature, which would not make sense if they are responding rapidly to air temperature changes, but this may also be interpreted as a shorter negative lag (see Figure S15), due to both being driven by temperature and the high-frequency dv/v responding more quickly than the soil temperature at 10 cm or greater depth.

Comparison of dv/v time series with CZO data after filtering out the diurnal signals (Figures 8 and S12) reveals correlations between non-cyclical and long-term events in these datasets. Many low and high dv/v events appear in both SPMS and SPVF, and several of the more prominent events are indicated by vertical lines in Figure 8. Large rain events, which are accompanied by increases in soil moisture and groundwater level, are often followed by drops in dv/v, at least at the higher frequencies. They are, however, also frequently accompanied by drops in air and soil temperature, making it difficult to distinguish hydrological and temperature effects. A notable velocity peak on March 30 (Figure 8, vertical line 1) is not associated with a major rain event but does coincide with a sharp peak in temperature.

The largest rain event of the study period occurred on May 12 and is particularly helpful in interpreting the results. In frequency bands from 30–60 Hz and higher, the negative dv/v excursion following the event exhibits double minima, with the first low point following shortly after peak rainfall and aligning with peak soil moisture and the second aligning approximately with the low point of soil temperature (vertical lines 4 and 5 in Figures 8 and 9). A similar double peak can be seen following another large rain event of April 14–15 (vertical lines 2 and 3 in Figures 8 and 9).

Longer-term (seasonal) changes are small (Figure 8a) but most frequency bands show a slight net increase in velocity over the spring, while the changes in October are more variable. The velocities at the end of the spring deployment and beginning of the fall deployment are similar in many frequency bands and do not show a consistent direction of offset where they differ. In comparison, air and soil temperature and evapotranspiration (as measured by latent heat flux) both rise during the spring deployment (Figures 8c and S12), while soil moisture and well water levels fall slightly (Figure 8c and e). Air and soil temperatures change only slightly between the end of the spring deployment and the beginning of the October deployment, while soil moisture, well water levels, and latent heat flux all drop substantially (Figures 8 and S12–13).

4. Discussion

4.1 Summary and Possible Causes of Seismic-Velocity Changes

Seismic ambient noise is a relatively new field of geophysics with the potential for continuous monitoring of small seismic-velocity changes in the subsurface. Such a tool has the potential to improve understanding of time-varying processes in the subsurface part of the critical zone, which is difficult to observe directly. In this study, we have applied the technique to closely spaced seismometers at higher frequencies than in previous work in order to investigate a range of near-surface depths (from ~1 m to 10s of m). Our intent was to identify the causes of seismic-velocity changes at these depths and the ability of ambient noise to detect time-varying processes in the critical zone.

We have successfully detected changes of less than 1% in the seismic velocities of coda waves embedded within the ambient-noise wavefield at very high frequencies that are sensitive to the shallow subsurface. We also created a one-dimensional velocity model for the shallow subsurface at mid-slope, which suggests that the upper 8–10 meters are highly porous, due to fracturing, chlorite weathering, or both, and are mostly unsaturated, with a less porous but more water-saturated zone below. Higher saturation above 4.5 m (Fig. 3e) may also indicate the presence of a shallow interflow zone (Sullivan, 2016) in the top few meters. Similarity between velocity change observations at mid-slope and valley floor sites and agreement of our 1D velocity model with borehole logs enhances confidence in our results. The velocity changes demonstrate i) diurnal cyclical variations, ii) short-term events (peaks or troughs) over hours to days, and iii) long-term seasonal changes over weeks to months. As discussed above, physical processes occurring in the critical zone that could hypothetically explain our results include changes in groundwater level and in water and gas saturation, temperature changes, and changes in air pressure, all of which are measured at the SSHCZO. Changes in dv/v are correlated with changes in environmental data, especially temperature, suggesting possible causal relationships.

The physical origin of seismic-velocity changes related to water movement is straightforward: addition or removal of water directly changes the medium through which the seismic waves pass. The effect of temperature is not as straightforward, however. Daily changes in temperature are limited to the very near surface (see the difference between 10 and 40 cm depths in Figure 6), but we observe diurnal velocity changes that correlate with temperature at low frequencies that are most sensitive to tens of meters depth (Figure 7). This fact suggests that direct heating and cooling of the rock is unlikely to be the cause of the velocity changes. Thermoelastic strain due to combined spatial and temporal variation of the temperature field over irregular topography can, however, extend much deeper than the actual temperature changes (Ben-Zion and Leary, 1986; Ben-Zion and Allam, 2013; Berger et al., 1975; Tsai, 2001). Therefore, this thermoelastic effect likely drives the temperature-related variations in velocity in our study.

Subsurface water movement is of substantial interest in critical zone science for its importance to life and to the evolution of the critical zone through processes such as weathering and soil formation. Such movement is therefore an important target of critical zone geophysics. To the extent that it can be detected with ambient noise, the method offers the potential to improve understanding of how variations in conditions at the surface can affect deeper phenomena. At least at Shale Hills, however, the water-related signal appears smaller than that related to thermoelastic effects, which may limit the applicability of the method to water-related questions. Whether thermoelastic strain affects the evolution of the critical zone (such as by promoting or inhibiting fracture formation) has not to our knowledge been studied and may be a worthwhile subject of future investigation given the strength of the signal we observe from that process.

4.2 Diurnal and Semidiurnal Variations

Our observation of a diurnal signal in dv/v is similar to the results of Mao et al. (2019), who used ambient noise MWCS to monitor hourly velocity variations at frequencies of 1–5 Hz on La Réunion Island. They attributed the diurnal signal there primarily to thermal effects and secondarily to tidal effects, based on spectral analysis. An important difference, however, is that they also saw clear semidiurnal and terdiurnal (3 cycles per day) signals, which they attributed to tidal and thermal effects respectively. In contrast, we see a faint semidiurnal signal in dv/v in only a few of our frequency bands and no terdiurnal signal. Our lack of a terdiurnal signal is consistent with our temperature data, which do not show a clear terdiurnal peak, while our lack of a strong semidiurnal signal indicates that tides are not a major factor in seismic-velocity changes at SSHCZO. It is not surprising that tidal signals are much weaker at the inland SSHCZO than on an island such as La Réunion.

The strong diurnal signal and much weaker to non-existent semidiurnal signal in the dv/v spectrograms (Figure 5) are most consistent with the air and soil temperature spectrograms in Figure 6, and these datasets correlate strongly with dv/v (Figure 7). Since the diurnal signal is present in all frequency bands and is especially clear at 10–20 Hz and 15–30 Hz (i.e., relatively low frequencies most sensitive to depths below 10 m), the relationship is inferred to be caused by the thermoelastic effect discussed above. The lag of 10–20, 15–30 and 20–40 Hz dv/v after soil temperature by no more than a few hours (Figure 7) can easily be explained by the thermoelastic effect, which predicts lag times on the order of hours for depths on the order of 10 meters (Richter et al., 2014). The shorter lag time for 5–10 Hz may indicate cycle-skipping in the cross-correlation if the real lag time is greater than 24 hours, although the lower correlation coefficient in this frequency band may simply indicate that this lag time is less meaningful. At high frequencies (30–60 Hz and above), lags between dv/v and air temperature are near zero (Figure 7). Since thermoelastic strains explain the lower frequency changes, a simple explanation is that the high frequencies are responding thermoelastically to temperature changes in the very top part of the soil that occur within less than an hour of air temperature changes.

The near-zero-lag correlation of high-frequency dv/v with air temperature also raises the possibility of direct thermal effects on the instruments at these frequencies. Previous work (Farrell et al., 2018; Johnson et al., 2019) has documented a temperature-dependent spectral modulation in nodal seismometers of the type used in this study, but this would not necessarily affect dv/v measurements. Any direct effect on the instruments should not change the cross-correlations if it is the same on all instruments, and it is likely to be averaged out among the different station pairs (36 in each subarray) if it is random. It appears likely, therefore, that we are seeing a real change in the medium through which seismic waves pass even at these high frequencies.

The strongest component of the latent heat flux, like temperature, is a diurnal signal (Figure 6), and it too correlates well with dv/v (Figure 7) Evapotranspiration can drive diurnal movement of water, at least above the water table (Harmon et al., 2020), which could drive the diurnal velocity variation. Another important feature of the latent heat flux data, however, is that it is highly seasonal. Specifically, these data show a strong increase in the amplitude of the diurnal and semidiurnal signals around the beginning of May, and a drop again sometime before October. This most likely corresponds to the growth of leaves (i.e., “leaf out”) and resulting increase in evapotranspiration. Some ambient-noise frequencies (mostly 10–20 and 15–30 Hz) show a sustained increase in the amplitude of dv/v in the later part of the spring, but these lower frequencies are likely to be most sensitive to depths below the water table, and the same signal is not seen at higher frequencies. While the presence of a seasonal change at some frequencies suggests that evapotranspiration-driven subsurface water movement could play a role in diurnal velocity variations, the greater overall similarity between the dv/v and temperature spectrograms suggests that the thermoelastic effect is the primary control on velocity changes. The high correlation between dv/v and latent heat flux may be explained if temperature is an underlying cause of variation in both measurements.

Overall, the spectrogram and cross-correlation analyses are consistent with the thermoelastic effect (driven by diurnal temperature changes in the soil) as the primary driver of the observed diurnal cycle in dv/v. Nonetheless, some of our observations are consistent with evapotranspiration-driven subsurface water movement as a possible secondary control on diurnal velocity variations.

4.3 Short-Term Non-Cyclic Events

As noted above, short-term, non-cyclic events seen in the lowpass-filtered dv/v in Figures 8 and 9 correspond with both rainfall events and high or low temperature events. Since diurnal temperature variations are a major driver of diurnal velocity variations, we expect that non-cyclic temperature changes would also drive non-cyclic velocity changes. The fact that storms often coincide with changes in temperature indicates that thermoelastic effects should be considered alongside hydrologic effects when ambient noise velocity changes are associated with precipitation events. Nonetheless, there is a clear physical reason to expect that water infiltration into the subsurface will also decrease Rayleigh wave velocity by reducing Vs. The negative dv/v excursions associated with rainfall events in Figures 8 and 9 are most apparent at the high frequencies that sample shallow depths. These depths are also those that are most impacted by infiltration of rainfall. In contrast, the thermoelastic effect would not necessarily be more prominent at high frequencies; in fact, the diurnal thermoelastic signals are most prominent at lower frequencies, so the same might be expected for non-cyclic events. As noted above, the rainfall event of May 12 is particularly illustrative, with two dv/v minima aligning with the maximum soil moisture and with the later minimum soil temperature (Figure 9). There is a slight double peak in the air temperature as well, but dv/v for the 30–60, 40–80, and 50–100 Hz bands reaches significantly lower values in the first minimum than the second, which does not match the air temperature but could be explained by superposition of a soil moisture effect on top of the air temperature effect. That this effect is more prominent at SPMS than at SPVF may be due to the much higher pre-storm soil moisture at 10 and 20 cm at the valley site (SPVF) as compared to the mid-slope (SPMS).

4.4 Long-Term Seasonal Changes

Long-term changes in dv/v over the period of this study are minor, but there is a slight overall increase during the spring in most frequency bands (Figure 8a), which could be explained by rising temperatures, falling groundwater levels, or extraction of water from the unsaturated zone by increasing evapotranspiration. All of these processes would be expected to cause seismic velocity to increase. The processes related to water movement, however, should show a sharp increase in velocity from the end of the spring deployment to the beginning of the October deployment. Such a sharp change is seen in the soil moisture, groundwater depth, and latent heat flux data but is not seen in the dv/v results. Offsets in dv/v from spring to fall are generally small and are not all in the same direction. If groundwater depth is the controlling factor, we would also expect to see a much greater change at SPMS than at SPVF, which we do not observe. Only temperature predicts a small change between the deployments at both sites. This result indicates that temperature is most likely the dominant control on the long-term velocity changes seen at the SSHCZO, although once again water-related changes may play a secondary role.

4.5 Applicability of Our Results to Other Sites

Our study presents an application of ambient noise coda wave analysis to shorter interstation distances and higher frequencies than we are aware of in previous work, but we expect that our methods could be applied at other critical zone sites. In considering how our results may apply more generally to other study areas, we note that the subsurface in Shale Hills consists of a thin (< 1 m) soil layer overlying fractured and weathered shale bedrock on a hillslope. Rayleigh waves, even at high frequencies, are thus most affected by seismic velocities below the soil layer. Sites with thicker soil layers or unconsolidated sediments may be affected differently. For instance, the effect of water saturation on interparticle stresses in unconsolidated sediments (Shen et al., 2016) as well as the potentially greater porosity and permeability of such sediments might produce a stronger response to water movement than is seen at Shale Hills. Further, topography plays a role in generating thermoelastic strain along with spatial variations in the temperature field and in rock properties (Ben-Zion and Leary, 1986), so its effect may be less pronounced in flatter terrain. Nonetheless, given the prominence of thermoelastic signals in our results, it is most likely that the effect will be widely observed as at least one component of critical zone seismic-velocity changes.

5. Conclusions

Our results demonstrate that changes in seismic velocity in the shallowest part of the critical zone can be detected at very high frequencies (up to at least 100–200 Hz) and at hourly resolution using cross-correlations of ambient seismic noise. These changes document how surface forcings propagate downward to tens of meters depth below the land surface. The seismic velocities respond to seasonal changes and show strong diurnal cycles and effects from meteorological events. At all timescales and at all studied frequencies, seismic-velocity variations are most clearly associated with changes in air and soil temperature. We therefore attribute most of the signal to the thermoelastic effect. In other words, temperature changes forced by insolation of the land surface cause elastic effects in the earth to tens of meters of depth or more that can be detected with these ambient-noise-related techniques. This effect can drive velocity changes well below the depths to which temperature changes propagate. The velocities also change because of secondary effects driven by water movements. Water-driven effects can be distinguished from the thermoelastic signal following rain events because we observe prominent double minima in seismic velocities. The sequence of minima is attributed first to rainfall infiltration, and then to a drop in soil temperature.

This study demonstrates the intriguing benefits of the application of ambient-noise seismology to time-lapse critical-zone studies. The methods used here detect changes in seismic velocities at depths relevant to critical-zone science without the need for repeated active-source experiments and at a higher temporal resolution than would be practical for an active-source study. The work also shows that to understand the complex array of changes in the near-subsurface, temperature must be monitored and its effects fully accounted for before ascribing observed velocity changes to changes in water content such as soil moisture, vadose zone moisture, or groundwater depth. Future studies should be aimed at distinguishing thermoelastic from hydrological effects. The thermoelastic effect that we observe occurs widely and is likely to be an important component of critical-zone seismic-velocity changes in many locations. However, more studies will be needed to generalize these results.

Finally, the good agreement between our one-dimensional Vs velocity model and nearby borehole sonic logs (Figure 3) supports the use of ambient noise in static imaging studies of the critical zone. Indeed, we are able to discern structure in shallower layers than interrogated by the sonic logs because the latter are limited by the depth of the water table and well casing. Therefore, even where borehole data are available, high-frequency ambient noise can reveal additional information. In our dispersion curves and in our analysis of velocity changes, we have observed meaningful ambient noise signals over a range of high frequencies from 10s to 100s of Hz, which in this location are sensitive to depths from ~1 to 10s of meters.

Acknowledgements

We thank the Incorporated Research Institutes for Seismology (IRIS) for providing the nodal seismometers, and Kyle Homman, Erica Lucas, and Lisa Ma for help with field work. We thank Charles Ammon for helpful conversations about surface wave analysis and Yuning Shi, David Eissenstat, Yuting He, and Qicheng Tang for discussions of critical zone processes. This research was conducted in Penn State's Stone Valley Forest, which is funded by the Penn State College of Agriculture Sciences, Department of Ecosystem Science and Management, and managed by the staff of the Forestlands Management Office. Financial support was provided by the Sensors in the Soils program (SitS) at the National Science Foundation Grant EAGER SitS #EAR 18-41568 to SLB. Funding for the CZO derives from NSF Critical Zone Observatory grants EAR 12-39285 and 13-31726 to SLB. Funding for some of the seismic measurements were provided by DOE OBES DE-FG02-05ER15675. We thank Marine Denolle, two anonymous reviewers, and the editors for their comments, which have significantly improved this manuscript.

Open Research

Data Availability Statement

The seismic data are archived by IRIS and are available at https://doi.org/10.7914/SN/XZ_2019 for the spring data and https://doi.org/10.7914/SN/5A_2019 for the fall data. The Shale Hills CZO hydrological and meteorological data are available from the CZO website at the following locations:

Evapotranspiration: http://www.czo.psu.edu/data_surfflux.html, Precipitation : http://www.czo.psu.edu/ShaleHills/SHSP_through_10_min_precip_level_0.html, SPVF Soil Moisture and Soil Temperature: http://www.czo.psu.edu/data_ghsmsh_spvf.html, SPMS Soil Moisture and Soil Temperature: http://www.czo.psu.edu/data_ghsmsh_spms.html, Well 5 Water Levels: http://www.czo.psu.edu/data/ShaleHills/wells/sh_well5.html, Well 7 Water Levels: http://www.czo.psu.edu/data/ShaleHills/wells/sh_well_7.html, CZMW8 Water Levels: http://www.czo.psu.edu/data_sh_CZMW8.html, and air temperature and air pressure: http://www.czo.psu.edu/data/ShaleHills/czmw8_baro_at.html. The msnoise program is available at http://www.msnoise.org/.

References

Berger, J., 1975. A note on thermoelastic strains and tilts. Journal of Geophysical Research 80(2), 274-277.

Bensen, G.D., Ritzwoller, M.H., Barmin, M.P., Levshin, A.L., Lin, F., Moschetti, M.P., Shapiro, N.M., and Yang, Y., 2007. Processing seismic ambient noise data to obtain reliable broad-band surface wave dispersion measurements. Geophysical Journal International 169, 1239-1260. doi: 10.1111/j.1365-246X.2007.03374.x

Ben-Zion, Y. and Allam, A.A., 2013. Seasonal thermoelastic strain and postseismic effects in Parkfield borehole dilatometers. Earth and Planetary Science Letters 379, 120-126. http://dx.doi.org/10.1016/j.epsl.2013.08.024

Ben-Zion, Y. and Leary, P., 1986. Thermoelastic strain in a half-space covered by unconsolidated material. Bulletin of the Seismological Society of America 76(5), 1447-1460.

Bodin, T., Sambridge, M., Tkalčić, H., Arroucau, P., Gallagher, K., and Rawlinson, N., 2012. Transdimensional inversion of receiver functions and surface wave dispersion. Journal of Geophysical Research 117, B02301. doi:10.1029/2011JB008560

Bonnefoy-Claudet, S., Cotton, F., and Bard, P.-Y., 2006. The nature of noise wavefield and its applications for site effects studies: A literature review. Earth Science Reviews 79, 205-227. doi:10.1016/j.earscirev.2006.07.004

Boué, P., Poli, P., Campillo, M., Pedersen, H., Briand, X., and Roux, P., 2013. Teleseismic correlations of ambient seismic noise for deep global imaging of the Earth. Geophysical Journal International 194, 844-848. doi: 10.1093/gji/ggt160

Brantley, S.L., DiBiase, R.A., Russo, T.A., Shi, Y., Lin, H., Davis, K.J., Kaye, M., Hill, L., Kaye, J., Eissenstat, D.M., Hoagland, B., Dere, A.L., Neal, A.L., Brubaker, K.M., and Arthur, D.K., 2016. Designing a suite of measurements to understand the critical zone. Earth Surface Dynamics 4, 211-235.

Brantley, S.L., Goldhaber, M.B., and Ragnarsdottir, K.V., 2007. Crossing disciplines and scales to understand the critical zone. Elements 3, 307-314.

Brantley, S.L. and Gu, X., 2020a. Shale Hills Well 5 Data (Level 1). [Data set.] Susquehanna Shale Hills Critical Zone Observatory, PA. http://www.czo.psu.edu/data/ShaleHills/wells/sh_well5.html (accessed 4/1/2020).

Brantley, S.L. and Gu, X., 2020b. Shale Hills Well 7 Data (Level 1). [Data set.] Susquehanna Shale Hills Critical Zone Observatory, PA. http://www.czo.psu.edu/data/ShaleHills/wells/sh_well_7.html (accessed 7/27/2020).

Brantley, S.L. and Gu, X., 2020c. Shale Hills CZMW 8 Groundwater Level and Water Temperature. [Data set.] Susquehanna Shale Hills Critical Zone Observatory, PA. http://www.czo.psu.edu/data_sh_CZMW8.html (accessed 7/27/2020).

Brantley, S.L. and Gu, X., 2020d. Shale Hills CZMW 8 Barometric Pressure and Air Temperature on South Planar Ridge Top. [Data set.] Susquehanna Shale Hills Critical Zone Observatory, PA. http://www.czo.psu.edu/data/ShaleHills/czmw8_baro_at.html (accessed 7/27/2020).

Brantley, S.L., Holleran, M.E., Jin, L., and Bazilevskaya, E., 2013. Probing deep weathering in the Shale Hills Critical Zone Observatory, Pennsylvania (USA): the hypothesis of nested chemical reaction fronts in the subsurface. Earth Surface Processes and Landforms 38, 1280-1298. doi: 10.1002/esp.3415

Brantley, S.L., White, T.S., West, N., Williams, J., Forsythe, B., Shapich, D., Kaye, J., Lin, H., Shi, Y., Kaye, M., Herndon, E., Davis, K., He, Y., Eissenstat, D., Weitzman, J., DiBiase, R.A., Li, L., Reed, W., Brubaker, K.M., Gu, X., 2018. Susquehanna Shale Hills Critical Zone Observatory: Shale Hills in the Context of Shaver's Creek Watershed. Vadose Zone Journal 17, 180092, doi: 180010.182136/vzj182018.180004.180092.

Bracewell, R.N., 1978. The Fourier Transform and its Applications, McGraw-Hill, 2nd edition, New York.

Brenguier, F., Campillo, M., Hadziioannou, C., Shapiro, N.M., Nadeau, R.M., and Larose, E., 2008. Postseismic relaxation along the San Andreas Fault at Parkfield from continuous seismological observations. Science 321, 1478-1481. doi: 10.1126/science.1160943

Brenguier, F., Shapiro, N.M., Campillo, M., Ferrazzini, V., Duputel, Z., Coutant, O., and Nercessian, A., 2008. Towards forecasting volcanic eruptions using seismic noise. Nature Geoscience 1, 126-130. doi:10.1038/ngeo104

Civilini, F., Savage, M.K., and Townend, J., 2020. Shear wave velocity changes induced by earthquakes and rainfall at the Rotokawa and Ngatamariki geothermal fields, Taupō Volcanic Zone, New Zealand. Geophysical Journal International 221, 97-114. doi: 10.1093/gji/ggz547

Clarke, D., Zaccarelli, L., Shapiro, N.M., and Brenguier, F., 2011. Assessment of resolution and accuracy of the Moving Window Cross Spectral technique for monitoring crustal temporal variations using ambient seismic noise. Geophysical Journal International 186, 867-882.

Clements, T. and Denolle, M.A., 2018. Tracking groundwater levels using the ambient seismic field. Geophysical Research Letters 45, 6459-6465. https://doi.org/10.1029/2018GL077706

Colombi, A., Chaput, J., Brenguier, F., Hillers, G., Roux, P., and Campillo, M., 2014. On the temporal stability of the coda of ambient noise correlations. Comptes Rendus Geoscience 346, 307-316. http://dx.doi.org/10.1016/j.crte.2014.10.002

Davis, K., 2020. Shale Hills Land & Atmosphere Flux Data [Data set]. Susquehanna Shale Hills Critical Zone Observatory, PA. http://www.czo.psu.edu/data_surfflux.html (accessed 3/27/2020).

Dziewonski, A., Bloch, S., and Landisman, M., 1969. A technique for the analysis of transient seismic signals. Bulletin of the Seismological Society of America 59(1), 427-444.

Eissenstat, D., Duncan, J., and Tang, Q., 2020. Shale Hills Ten Minute Through-fall Precipitation - Level 0 [Data set.] Susquehanna Shale Hills Critical Zone Observatory, PA. http://www.czo.psu.edu/ShaleHills/SHSP_through_10_min_precip_level_0.html (accessed 2/14/2020).

Farrell, J., Wu, S.-M., Ward, K.M., and Lin, F.-C., 2018. Persistent noise signal in the FairfieldNodal three-component 5-Hz geophones. Seismological Research Letters, 89 (5), 1609-1617. doi: 10.1785/0220180073

Feng, S., Sugiyama, T., Yamanaka, H., 2001. Application of sensitivity analysis to array design for microtremor array survey. Proceedings of the 104th SEGJ Conference, pp. 35–39.

Fores, B., Champollion, C., Mainsant, G., Albaric, J., and Fort, A., 2018. Monitoring saturation changes with ambient seismic noise and gravimetry in a karst environment. Vadose Zone Journal 17:170163. doi:10.2136/vzj2017.09.0163

Gassenmeier, M., Sens-Schönfelder, C., Delatre, M., and Korn, M., 2015. Monitoring of environmental influences on seismic velocity at the geological storage site for CO_2 in Ketzin (Germany) with ambient seismic noise. Geophysical Journal International 200, 524-533. doi: 10.1093/gji/ggu413

Gao, C. and Lekić, V., 2018. Consequences of parametrization choices in surface wave inversion: insights from transdimensional Bayesian methods. Geophysical Journal International 215, 1037-1063. doi: 10.1093/gji/ggy310

Gu, X., Mavko, G., Ma, L., Oakley, D., Accardo, N., Carr, B.J., Nyblade, A.A., and Brantley, S.L., 2020. Seismic refraction tracks porosity generation and possible CO_2 production at depth under a headwater catchment. PNAS. https://www.pnas.org/cgi/doi/10.1073/pnas.2003451117

Guillemot, A., Helmstetter, A., Larose, É., Baillet, L., Garambois, S., Mayoraz, R., and Delaloye, R., 2020. Seismic monitoring in the Gugla rock glacer (Switzerland): ambient noise correlation, microseismicity and modelling. Geophysical Journal International 221 (3), 1719-1735. doi: 10.1093/gji/ggaa097

Guo L., Chen J. and Lin H., 2014. Subsurface lateral preferential flow network revealed by time-lapse ground-penetrating radar in a hillslope. Water Resour. Res. 50, 9127–9147. doi:10.1002/2013WR014603.Harmon, R., Barnard, H.R., and Singha, K., 2020. Water table depth and bedrock permeability control magnitude and timing of transpiration-induced diel fluctuations in groundwater. Water Resources Research 56, e2019WR025967. https://doi.org/10.1029/2019WR025967

Herrmann, R.B., 2013. Computer programs in seismology: An evolving tool for instruction and research. Seismological Research Letters 84 (6), 1081-1088. doi: 10.1785/0220110096

Hillers, G., Ben-Zion, Y., Campillo, M., and Zigone, D., 2015. Seasonal variations of seismic velocities in the San Jacinto fault area observed with ambient seismic noise. Geophysical Journal International 202, 920-932. doi: 10.1093/gji/ggv151

Hillers, G., Campillo, M., Brenguier, F., Moreau, L, Agnew, D.C., and Ben-Zion, Y., 2019. Seismic velocity change patterns along the San Jacinto fault zone following the 2010 M7.2 El Mayor-Cucapah and M5.4 Collins Valley earthquakes. Journal of Geophysical Research: Solid Earth 124, 7171-7192. https://doi.org/10.1029/2018JB017143

Hillers, G., Campillo, M., and Ma, D.-F., 2014. Seismic velocity variations at TCDP are controlled by MJO driven precipitation pattern and high fluid discharge properties. Earth and Planetary Science Letters 391, 121-127. http://dx.doi.org/10.1016/j.epsl.2014.01.040

Holbrook, W.S., Riebe, C.S., Elwaseif, M., Hayes, J.L., Basler-Reeder, K., Harry, D.L., Malazian, A., Dosseto, A., Hartsough, P.C., and Hopmans, J.W., 2014. Earth surface processes and landforms 39, 366-380.

James, S.R., Knox, H.A., Abbott, R.E., Panning, M.P., and Screaton, E.J., 2019. Insights into permafrost and seasonal active-layer dynamics from ambient seismic noise monitoring. Journal of Geophysical Research: Earth Surface 124, 1798-1816. https://doi.org/10.1029/2019JF005051

James, S.R., Knox, H.A., Abbott, R.E., and Screaton, E.J., 2017. Improved moving window cross-spectral analysis for resolving large temporal seismic velocity changes in permafrost. Geophysical Research Letters 44, 4018-4026. doi:10.1002/2016GL072468

Jin, L., Andrews, D.M., Holmes, G.H., Lin, H., and Brantley, S.L., 2011. Opening the “Black Box”: Water chemistry reveals hydrological controls on weathering in the Susquehanna Shale Hills Critical Zone Observatory. Vadose Zone Journal 10, 928-942. doi:10.2136/vzj2010.0133

Jin, L., Ravella, R., Ketchum, B., Bierman, P.R., Heaney, P., White, T., and Brantley, S.L., 2010. Mineral weathering and elemental transport during hillslope evolution at the Susquehanna/Shale Hills Critical Zone Observatory. Geochimica et Cosmochimica Acta 74, 3669-3691. doi:10.1016/j.gca.2010.03.036

Jin, L., Rother, G., Cole, D.R., Mildner, D.F.R., Duffy, C.J., and Brantley, S.L., 2011. Characterization of deep weathering and nanoporosity development in shale – A neutron study. American Mineralogist 96, 498-512. doi: 10.2138/am.2011.3598

Johnson, C.W., Vernon, F., Nakata, N., and Ben-Zion, Y., 2019. Atmospheric processes modulating noise in Fairfield Nodal 5 Hz geophones. Seismological Research Letters 90 (4), 1612-1618. doi: 10.1785/0220180383

Joubert, Anaëlle, Le Feuvre, M., and Côte, P., 2018. Passive monitoring of a sea dike during a tidal cycle using sea waves as a seismic noise source. Geophysical Journal International 214, 1364-1378. doi: 10.1093/gji/ggy180

Keifer, I., Dueker, K., and Chen, P., 2019. Ambient Rayleigh wave field imaging of the critical zone in a weathered granite terrane. Earth and Planetary Science Letters 510, 198-208. https://doi.org/10.1016/j.epsl.2019.01.015

Kim, D., and Lekic, V., 2019. Groundwater variations from autocorrelation and receiver functions. Goephysical Research Letters 46. https://doi.org/10.1029/2019GL084719

Lecocq, T., Caudron, C., and Brenguier, F., 2014. MSNoise, a Python Package for Monitoring Seismic Velocity Changes Using Ambient Seismic Noise. Seismological Research Letters 85 (3), 715-726. doi: 10.1785/0220130073

Lecocq, T., Longuevergne, L., Pedersen, H.A., Brenguier, F., and Stammler, K., 2017. Monitoring ground water storage at mesoscale using seismic noise: 30 years of continuous observation and thermo-elastic and hydrological modeling. Scientific Reports 7, 14241. doi: 10.1038/s41598-017-14468-9

Levshin, A.L., and Ritzwoller, M.H., 2001. Automated detection, extraction, and measurement of regional surface waves. Pure and Applied Geophysics 158, 1531-1545.

Li, H. and Eissenstat, D., 2020a. Shale Hills Soil Moisture, Electrical Conductivity, & Soil Temperature Data - South Planar Valley Floor (SPVF) Site. [Data set.] Susquehanna Shale Hills Critical Zone Observatory, PA. http://www.czo.psu.edu/data_ghsmsh_spvf.html (accessed 3/20/2020).

Li, H. and Eissenstat, D., 2020b. Shale Hills Soil Moisture, Electrical Conductivity, & Soil Temperature Data - South Planar Mid-Slope (SPMS) Site. [Data set.] Susquehanna Shale Hills Critical Zone Observatory, PA. http://www.czo.psu.edu/data_ghsmsh_spms.html (accessed 3/20/2020).

Lin H., 2006/ Temporal stability of soil moisture spatial pattern and subsurface preferential flow pathways in the Shale Jills catchment. Vadose Zone J. 5, 317–340. doi:10.2136/vzj2005.0058.

Lin, F.-C., Moschetti, M.P., and Ritzwoller, M.H., 2008. Surface wave tomography of the western United States from ambient seismic noise: Rayleigh and Love wave phase velocity maps. Geophysical Journal International 173, 281-298. doi: 10.1111/j.1365-246X.2008.03720.x

Liu, Z., Huang, J., He, P., and Qi, J., 2018. Ambient noise monitoring of seismic velocity around the Longmenshan fault zone from 10 years of continuous observation. Journal of Geophysical Research: Solid Earth 123, 8979-8994. https://doi.org/10.1029/2018JB015986

Luo, Y., Xia, J., Xu, Y., and Zeng, C., 2011. Analysis of group-velocity dispersion of high-frequency Rayleigh waves for near-surface applications. Journal of Applied Geophysics 74, 157-165. doi:10.1016/j.jappgeo.2011.04.002

Luo, Y., Yang, Y., Xu, Y., Xu, H., Zhao, K., and Wang, K., 2015. On the limitations of interstation distances in ambient noise tomography. Geophysical Journal International 201, 652-661.

Mao, S., Campillo, M., van der Hilst, R.D., Brenguier, F., Stehly, L., and Hillers, G., 2019. High temporal resolution monitoring of small variations in crustal strain by dense seismic arrays. Geophysical Research Letters 46, 128-137. https://doi.org/10.1029/2018GL079944

Meier, U., Shapiro, N.M., and Brenguier, F., 2010. Detecting seasonal variations in seismic velocities within Los Angeles basin from correlations of ambient seismic noise. Geophysical Journal International 181, 985-996. doi: 10.1111/j.1365-246X.2010.04550.x

Mordret, A., Courbis, R., Brenguier, F., Chmiel, M., Garambois, S., Mao, S., Boué, P., Campman, X., Lecocq, T., Van der Veen, W., and Hollis, D., 2020. Noise-based ballistic wave passive seismic monitoring – Part 2: surface waves. Geophysical Journal International 221 (1), 692-705. https://doi.org/10.1093/gji/ggaa016

Mordret, A., Landès, M., Shapiro, N.M., Singh, S.C., and Roux, P., 2014. Ambient noise surface wave tomography to determine the shallow shear velocity structure at Valhall: depth inversion with a Neighbourhood Algorithm. Geophysical Journal International 198, 1514-1525. doi: 10.1093/gji/ggu217

Moreau, L., Stehly, L., Boué, P., Lu, Y., Larose, E., and Campillo, M., 2017. Improving ambient noise correlation functions with an SVD-based Wiener filter Geophysical Journal International 211, 418-426. doi: 10.1093/gji/ggx306

Nakata, N., Chang, J.P., Lawrence, J.F., and Boué, P., 2015. Body wave extraction and tomography at Long Beach, California, with ambient-noise interferometry. Journal of Geophysical Research: Solid Earth 120, 1159-1173. doi:10.1002/2015JB011870

Nyblade, A., 2019a. Shale Hills Critical Zone Observatory Mini-Array Experiment. [Data set.] International Federation of Digital Seismograph Networks. https://doi.org/10.7914/SN/XZ_2019

Nyblade, A., 2019b. Shale Hills Critical Zone Observatory Mini-Array 2 Experiment. [Data set.] International Federation of Digital Seismograph Networks. https://doi.org/10.7914/SN/5A_2019

Olivier, G. and Brenguier, F., 2016. Interpreting seismic velocity changes observed with ambient seismic noise correlations. Interpretation, 4(3), SJ77-SJ85. http://dx.doi.org/10.1190/INT-2015-0203.1

Pan, Y., Schaneng, S., Steinweg, T., and Bohlen, T., 2018. Estimating S-wave velocities from 3D 9-component shallow seismic data using local Rayleigh-wave dispersion curves – A field study. Journal of Applied Geophysics 159, 532-539. https://doi.org/10.1016/j.jappgeo.2018.09.037\

Parsekian, A.D., Singha, K., Minsley, B.J., Holbrook, W.S., and Slater, L., 2015. Multiscale geophysical imaging of the critical zone. Reviews of Geophysics 53, 1-26. doi:10.1002/2014RG000465.

Ping, P., Chu, R., Zhang, Y., and Xie, J., 2020. Enhancing signal-to-noise ratios of high-frequency Rayleigh waves extracted from ambient seismic noises in topographic region. Bulletin of the Seismological Society of America 110, 793-802. doi: 10.1785/0120190177

Picozzi, M., Parolai, S., Bindi, D., and Strollo, A., 2009. Characterization of shallow geology by high-frequency seismic noise tomography. Geophysical Journal International 176, 164-174. doi: 10.1111/j.1365-246X.2008.03966.x

Pilz, M., Parolai, S., and Bindi, D., 2013. Three-dimensional passive imaging of complex seismic fault systems: evidence of surface traces of the Issyk-Ata fault (Kyrgyzstan). Geophysical Journal International 194, 1955-1965. doi: 10.1093/gji/ggt214

Pilz, M., Parolai, S., Bindi, D., Saponaro, A., and Abdybachaev, U., 2014. Combining seismic noise techniques for landslide characterization. Pure and Applied Geophysics 171, 1729-1745. DOI 10.1007/s00024-013-0733-3

Pilz, M., Parolai, S., Picozzi, M., and Bindi, D., 2012. Three-dimensional shear wave velocity imaging by ambient seismic noise tomography. Geophysical Journal International 189, 501-512. doi: 10.1111/j.1365-246X.2011.05340.x

Planès, T., Rittgers, J.B., Mooney, M.A., Kanning, W., and Draganov, D., 2017. Monitoring the tidal response of a sea levee with ambient seismic noise. Journal of Applied Geophysics 138, 255-263. http://dx.doi.org/10.1016/j.jappgeo.2017.01.025

Poupinet, G., Ellsworth, W.L., and Frechet, J., 1984. Monitoring velocity variations in the crust using earthquake doublets: An application to the Calaveras Fault, California. Journal of Geophysical Research 89 (B7), 5719-5731.

Qiu, H., Hillers, G., and Ben-Zion, Y., 2020. Temporal changes of seismic velocities in the San Jacinto Fault zone associated with the 2016 M_w 5.2 Borrego Springs earthquake. Geophysical Journal International 220, 1536-1554.

Richter, T., Sens-Schönfelder, C., Kind, R., and Asch, G., 2014. Comprehensive observation and modeling of earthquake and temperature-related seismic velocity changes in northern Chile with passive image interferometry. Journal of Geophysical Research: Solid Earth. 119, 4747-4765. doi:10.1002/2013JB010695

Rivet, D., Brenguier, F., and Cappa, F., 2015. Improved detection of preeruptive seismic velocity drops at the Piton de la Fournaise volcano. Geophysical Research Letters 42, 6332-6339. doi:10.1002/2015GL064835

Sabra, K.G., Gerstoft, P., Roux, P., and Kuperman, W.A., 2005. Surface wave tomography from microseisms in Southern California. Geophysical Research Letters 32, L14311. doi:10.1029/2005GL023155

Sabra, K.G., Gerstoft, P., Roux, P., Kuperman, W.A., and Fehler, M.C., 2005a. Extracting time-domain Green's function estimates from ambient seismic noise. Geophysical Research Letters 32, L03310. doi:10.1029/2004GL021862

Seats, K.J., Lawrence, J.F., and Prieto, G.A., 2012. Improved ambient noise correlation functions using Welch's method. Geophysical Journal International 188, 513-523. doi: 10.1111/j.1365-246X.2011.05263.x

Sens-Schönfelder, C. and Wegler, U., 2006. Passive image interferometry and seasonal variations in seismic velocities at Merapi Volcano, Indonesia. Geophysical Research Letters 33, L21302.

Shapiro, N.M. and Campillo, M., 2004. Emergence of broadband Rayleigh waves from correlations of the ambient seismic noise. Geophysical Research Letters 31, L07614. doi:10.1029/2004GL019491, 2004

Shapiro, N.M., Campillo, M., Stehly, L., and Ritzwoller, M.H., 2005. High-resolution surface-wave tomography from ambient seismic noise. Science 307, 1615-1618. DOI: 10.1126/science.1108339

Shen, J., Crane, J.M., Lorenzo, J.M., and White, C.D., 2016. Seismic velocity prediction in shallow (<30 m) partially saturated, unconsolidated sediments using effective medium theory. Journal of Environmental and Engineering Geophysics 21 (2), 67-78. DOI: 10.2113/JEEG21.2.67

Sullivan, P.L., Hynek, S.A., Gu, X., Singha, K., White, T., West, N., Kim, H., Clarke, B., Kirby, E., Duffy, C., and Brantley, S.L., 2016. Oxidative dissolution under the channel leads geomorphological evolution at the Shale Hills catchment. American Journal of Science 316, 981-1026. DOI 10.2475/10.2016.02

Takano, T., Nishimura, T., Nakahara, H., Ohta, Y., and Tanaka, S., 2014. Seismic velocity changes caused by the Earth tide: Ambient noise correlation analyses of small-array data. Geophysical Research Letters 41, 6131-6136. doi:10.1002/2014GL060690

Tang, Q., Duncan, J.M., Guo, L., Lin, H., Xiao, D., and Eissenstat, D.M., 2020. On the controls of preferential flow in soils of different hillslope position and lithological origin. Hydrological Processes 34, 4295-4306. https://doi.org/10.1002/hyp.13883

Tsai, V.C., 2011. A model for seasonal changes in GPS positions and seismic wave speeds due to thermoelastic and hydrologic variations. Journal of Geophysical Research 116, B04404. http://dx.doi.org/10.1016/j.epsl.2013.08.024

Viens, L., Denolle, M.A., Hirata, N., and Nakagawa, S., 2018. Complex near-surface rheology inferred from the response of greater Tokyo to strong ground motions. Journal of Geophysical Research: Solid Earth 123, 5710-5729.

Viens, L. and Van Houtte, C., 2020. Denoising ambient seismic field correlation functions with convolutional autoencoders. Geophysical Journal International 220, 1521-1535. doi: 10.1093/gji/ggz509

Voisin, C., Garambois, S., Massey, C., and Brossier, R., 2016. Seismic noise monitoring of the water table in a deep-seated slow-moving landslide. Interpretation, 4(3), SJ67-SJ76.

Wang, Q.-Y., Brenguier, F., Campillo, M., Lecointre, A., Takeda, T., and Aoki, Y., 2017. Seasonal crustal seismic velocity changes throughout Japan. Journal of Geophysical Research: Solid Earth 122, 7987-8002. https://doi.org/10.1002/2017JB014307

Wang, W., Chen, P., Keifer, I., Dueker, K., Lee, E.-J., Mu, D., Jiao, J., Zhang, Y., and Carr, B., 2019. Weathering front under a granite ridge revealed through full-3D seismic ambient-noise tomography. Earth and Planetary Science Letters 509, 66-77. https://doi.org/10.1016/j.epsl.2018.12.038

Wegler, U. and Sens-Schönfelder, 2007. Fault zone monitoring with passive image interferometry. Geophysical Journal International 168, 1029-1033. doi: 10.1111/j.1365-246X.2006.03284.x

Zigone, D., Ben-Zion, Y., Campillo, M. and Roux, P., 2015. Seismic tomography of the Southern California plate boundary region from noise-based Rayleigh and love waves. Pure and Applied Geophysics 172, 1007-1032. doi: 10.1007/s00024-014-0872-1

References for Supporting Information

Obermann, A., Planès, T., Larose, E., Sens-Schönfelder, C., and Campillo, M., 2013. Depth sensitivity of seismic coda waves to velocity perturbations in an elastic heterogeneous medium. Geophysical Journal International 194, 372-382. doi: 10.1093/gji/ggt043

Obermann, A., Planès, T., Hadziioannou, C., and Campillo, M., 2016. Lapse-time-dependent coda-wave depth sensitivity to local velocity perturbations in 3-D heterogeneous elastic media. Geophysical Journal International 207, 59-66. doi: 10.1093/gji/ggw264

Figure Captions

Figure 1: Locations of nodes and other instruments used in this study within the Shale Hills watershed. SPMS and SPVF are the South Planar Transect mid-slope and valley floor instrumentation sites. CZMW1, 10, and 8 are wells. FTAN is Frequency-Time Analysis (see section 2.4). GroundHOG is Ground Hydrological Observation Gear. Inset: Location of the Shale Hills catchment within the SSHCZO in Pennsylvania.

Figure 2: Example cross-correlation filtered between (a) 18–42 Hz, (b) 45–105 Hz, and (c) 90–210 Hz, which are the filters used for the MWCS analysis frequency bands of 20–40 Hz, 50–100 Hz, and 100–200 Hz, respectively. Blue shading indicates the expected time window for the direct arrival, assuming a velocity in the range 100–2500 m/s, and red shading indicates the coda window used for MWCS analysis. The nodes used for this correlation are those in the NW and SE corners of the square of red symbols at SPMS in Figure 1, with an interstation distance of 13.7 m. The cross-correlations are stacked over the entire spring deployment, as used for FTAN and the MWCS reference stack.

Figure 3: (a) Dispersion images and the group-velocity dispersion curve for Rayleigh waves in the vicinity of SPMS. (b) The dispersion images and the dispersion curve after applying phase-matched filtering. Alternate versions of a and b with a linear frequency scale can be found in Figure S2. (c) A plot of the one-dimensional shear-wave velocity model fit to the final dispersion curve (black line in b) in comparison to sonic log velocities from three wells in the catchment. The solid line is the mean velocity at each depth and the dotted lines show the 95% confidence intervals. (d and e) Porosity and mean values of water saturation (with 95% confidence intervals) calculated using the rock-physics model of Gu et al. (2020). These are not modeled above 2.5 m because the rock-physics model may not be applicable in the very near surface and especially in the soil. (f) Sensitivity curves for Rayleigh-wave phase velocity at different frequencies based on the mean velocity model. To calculate the sensitivity curves, the velocity model is discretized into 0.25 m thick layers and V_S in each layer is perturbed by 10% with V_P and density held constant. (Sensitivities for 5, 10, 15, and 20 Hz are too low to plot on the same scale and are shown in Figures S6 and S7.) The estimated depths of the water table and base of the chlorite-weathering zone (blue and tan horizontal lines, respectively) at SPMS are the averages of valley floor and ridge top values as discussed in the main text.

Figure 4: Example dv/v time series from MWCS analysis for two different frequency bands at SPMS and SPVF. Arrows indicate examples of features that are seen at both SPMS and SPVF,

highlighting the similarity between the results at the two locations. Plots for all ten frequency bands can be found in supporting figures S8–9.

Figure 5: Spectrograms of hourly dv/v (blue lines in Figures 4 and S8–9). High power spectral density (PSD), as indicated by yellow colors, shows the dominant frequencies in the dv/v time-series and how they change over the course of the deployment. Spectrograms are calculated using a 7-day moving window. PSD is normalized separately for each spectrogram so that they can be displayed with the same scale. Depth ranges in parentheses indicate the estimated depths at which each frequency is most sensitive to changes in Vs (Figure 3f and Table S1) for the minimum and maximum frequencies in each band. Note, however, that each frequency will be sensitive to some degree to a large range of depths and that the depths for 20 Hz and 30 Hz are particularly uncertain, as discussed in supporting Text S3.

Figure 6: Spectrograms of Shale Hills environmental data. These were made in the same way as those of dv/v in Figure 5.

Figure 7: Lag times and magnitude of correlation coefficient for cross-correlations of dv/v and environmental datasets. Data are bandpass filtered between 0.8 and 1.2 cycles / day to isolate the diurnal signal and are cross-correlated in 7-day-long, 50%-overlapping windows, which are then stacked together. Circles are for dv/v from SPMS and triangles are from SPVF.

Figure 8: Comparison of (a) dv/v and (b–e) environmental datasets. All datasets (except precipitation) have been lowpass filtered at 0.8 cycles/day to remove diurnal variations. For dv/v, soil moisture, and soil temperature, solid lines are data from SPMS and dashed lines are data from SPVF. (For dv/v, these are almost identical much of the time.) The numbered vertical dashed lines mark dv/v excursions discussed in the text that are thought to be attributable to the effects of temperature (red) or water (blue). The supporting information contains similar running means for latent heat flux and air pressure (Figure S12), as well as the hourly data from which the running means are derived (Figures S8–9 and S13).

Figure 9: Comparison of dv/v and environmental datasets (lowpass filtered as in Figure 8) around the times of major rain events. The numbered lines highlight the double minima with blue indicating the minima attributed at least partly to water and red the ones attributed to temperature. All time-series except precipitation have been lowpass filtered to remove the diurnal signal. The unfiltered time-series can be seen in Figure S14.

Figure1.

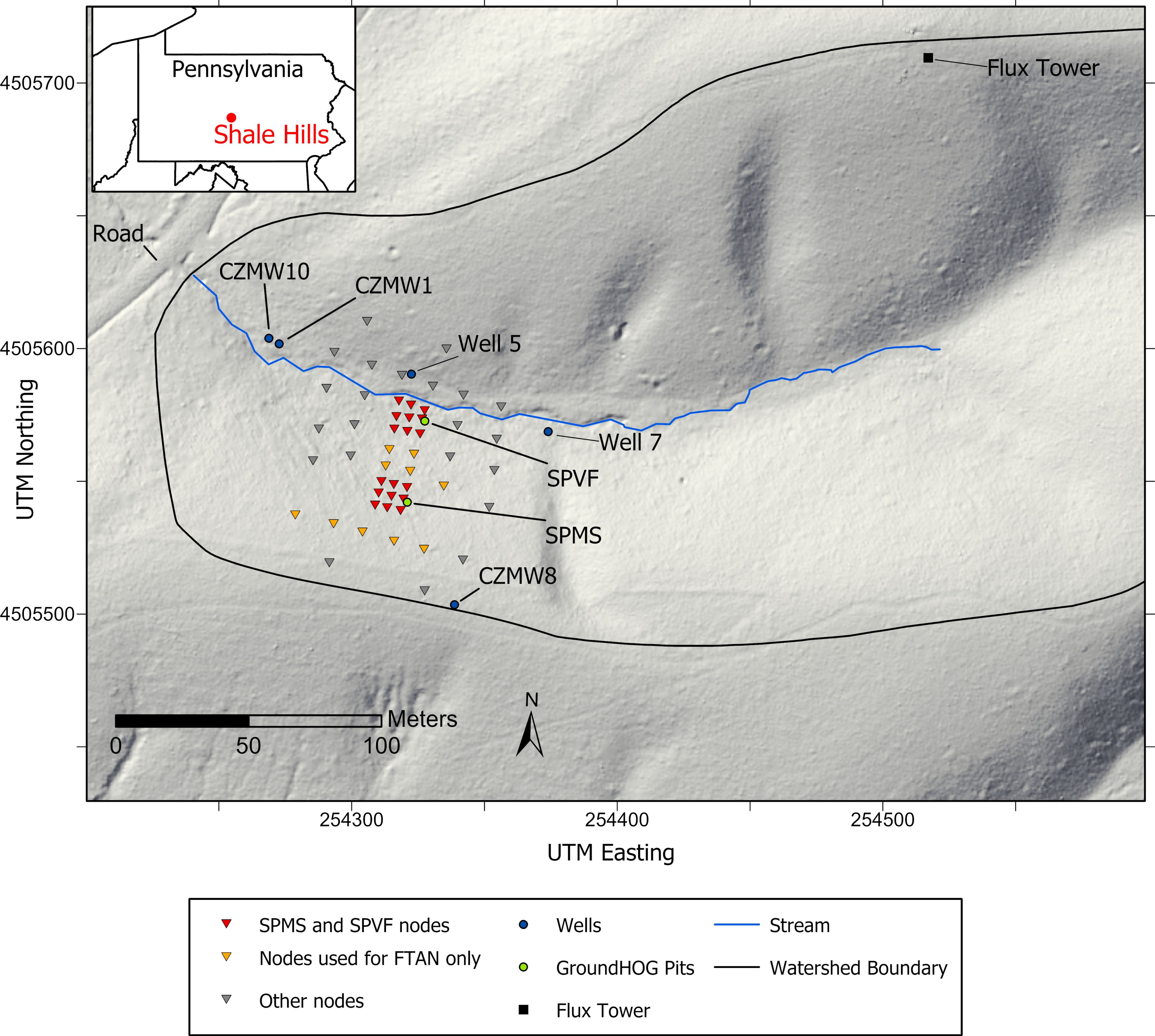
Pennsylvania
Shale Hills
Flux Tower
Road
CZMW10
CZMW1
Well 5
Well 7
SPVF
SPMS
CZMW8
4505700
4505600
4505500
UTM Northing
254300
254400
254500
UTM Easting
0
50
100
Meters
N
SPMS and SPVF nodes
Nodes used for FTAN only
Other nodes
Wells
GroundHOG Pits
Flux Tower
Stream
Watershed Boundary

Figure2.

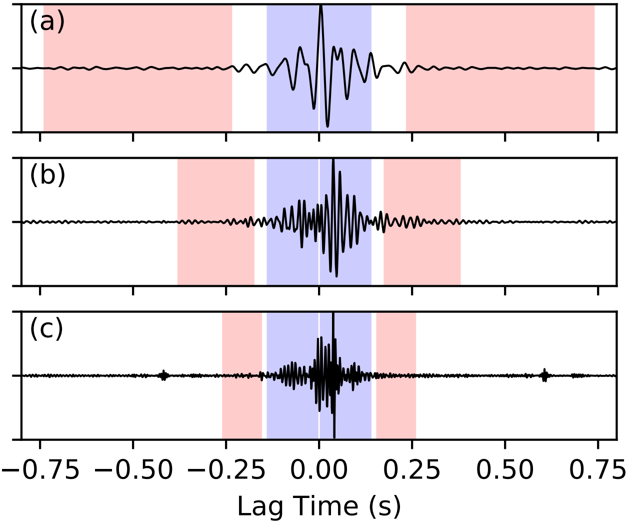
(a)
(b)
(c)
−0.75
−0.50
−0.25
0.00
0.25
0.50
0.75
Lag Time (s)

Figure3.

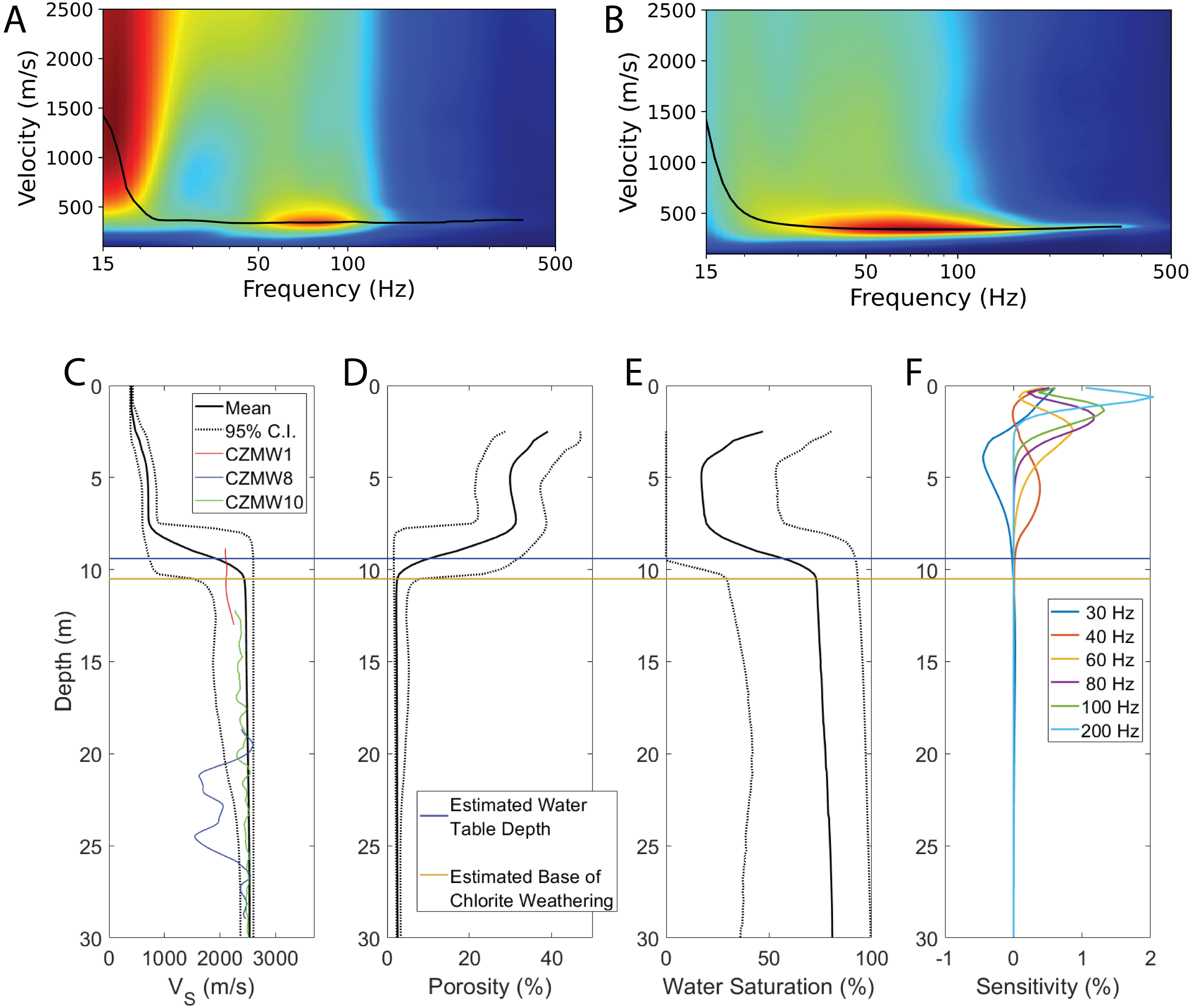
A
Velocity (m/s)
2500
2000
1500
1000
500
15
50
100
500
Frequency (Hz)
B
Velocity (m/s)
2500
2000
1500
1000
500
15
50
100
500
Frequency (Hz)
C
Mean
95% C.I.
CZMW1
CZMW8
CZMW10
Depth (m)
0
5
10
15
20
25
30
0
1000
2000
3000
V_S (m/s)
D
0
5
10
15
20
25
30
0
20
40
Porosity (%)
Estimated Water Table Depth
Estimated Base of Chlorite Weathering
E
0
5
10
15
20
25
30
0
50
100
Water Saturation (%)
F
0
5
10
15
20
25
30
30 Hz
40 Hz
60 Hz
80 Hz
100 Hz
200 Hz
-1
0
1
2
Sensitivity (%)

Figure4.

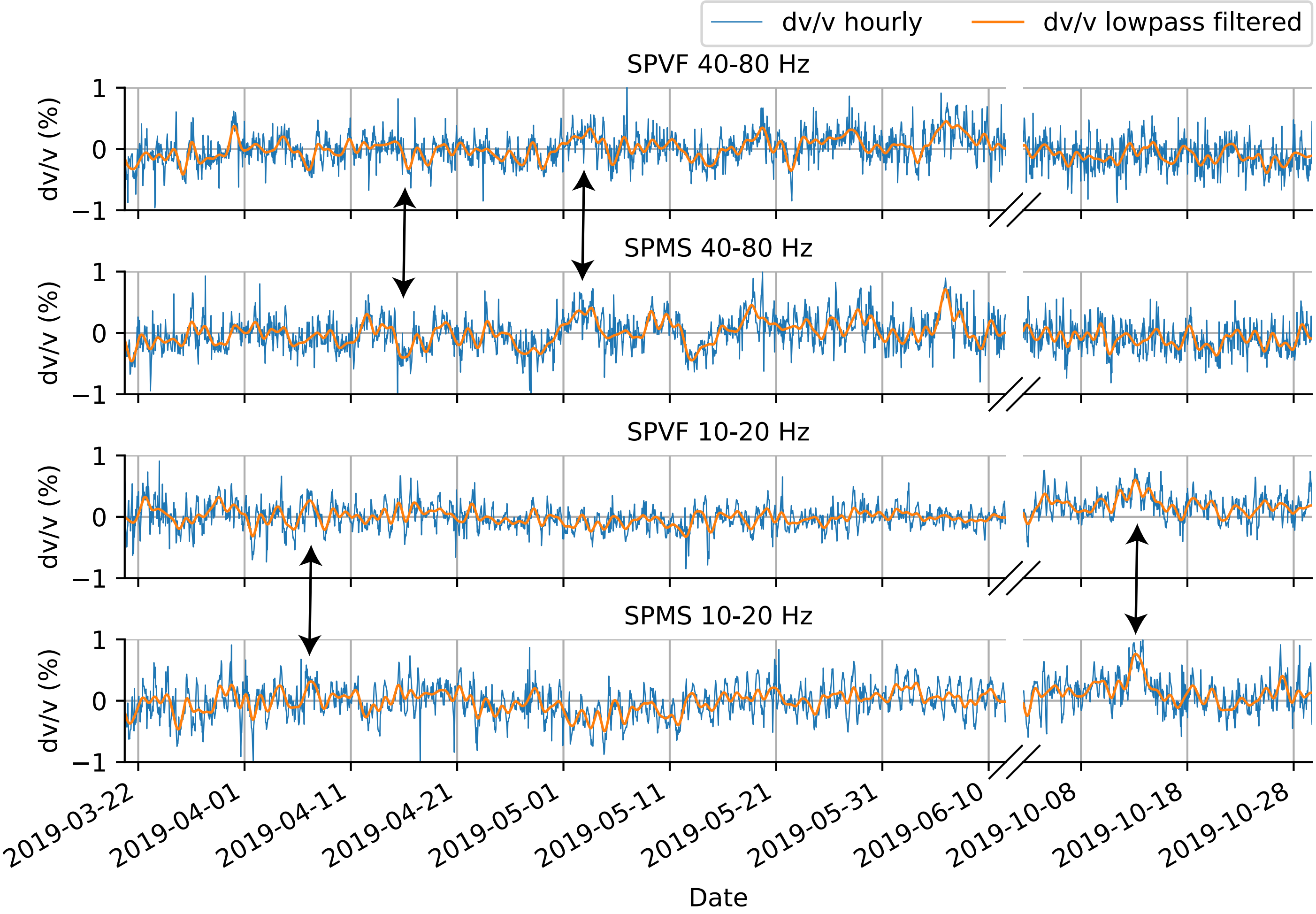
dv/v hourly
dv/v lowpass filtered
SPVF 40-80 Hz
SPMS 40-80 Hz
SPVF 10-20 Hz
SPMS 10-20 Hz
dv/v (%)
1
0
−1
2019-03-22
2019-04-01
2019-04-11
2019-04-21
2019-05-01
2019-05-11
2019-05-21
2019-05-31
2019-06-10
2019-10-08
2019-10-18
2019-10-28
Date

Figure5.

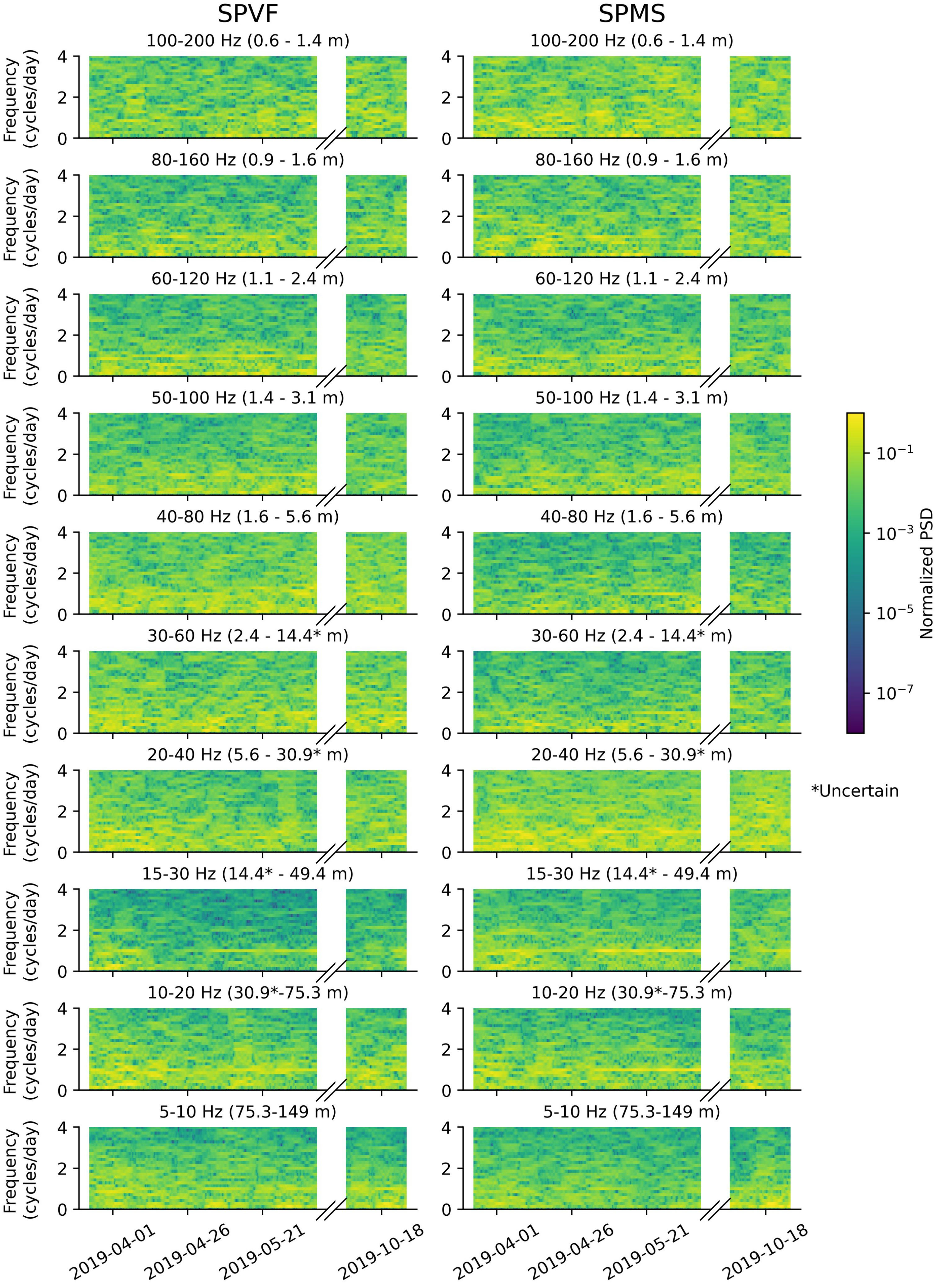
SPVF
SPMS
100-200 Hz (0.6 - 1.4 m)
80-160 Hz (0.9 - 1.6 m)
60-120 Hz (1.1 - 2.4 m)
50-100 Hz (1.4 - 3.1 m)
40-80 Hz (1.6 - 5.6 m)
30-60 Hz (2.4 - 14.4* m)
20-40 Hz (5.6 - 30.9* m)
15-30 Hz (14.4* - 49.4 m)
10-20 Hz (30.9*-75.3 m)
5-10 Hz (75.3-149 m)
Frequency (cycles/day)
0
2
4
2019-04-01
2019-04-26
2019-05-21
2019-10-18
Normalized PSD
10^{-1}
10^{-3}
10^{-5}
10^{-7}
*Uncertain

Figure6.

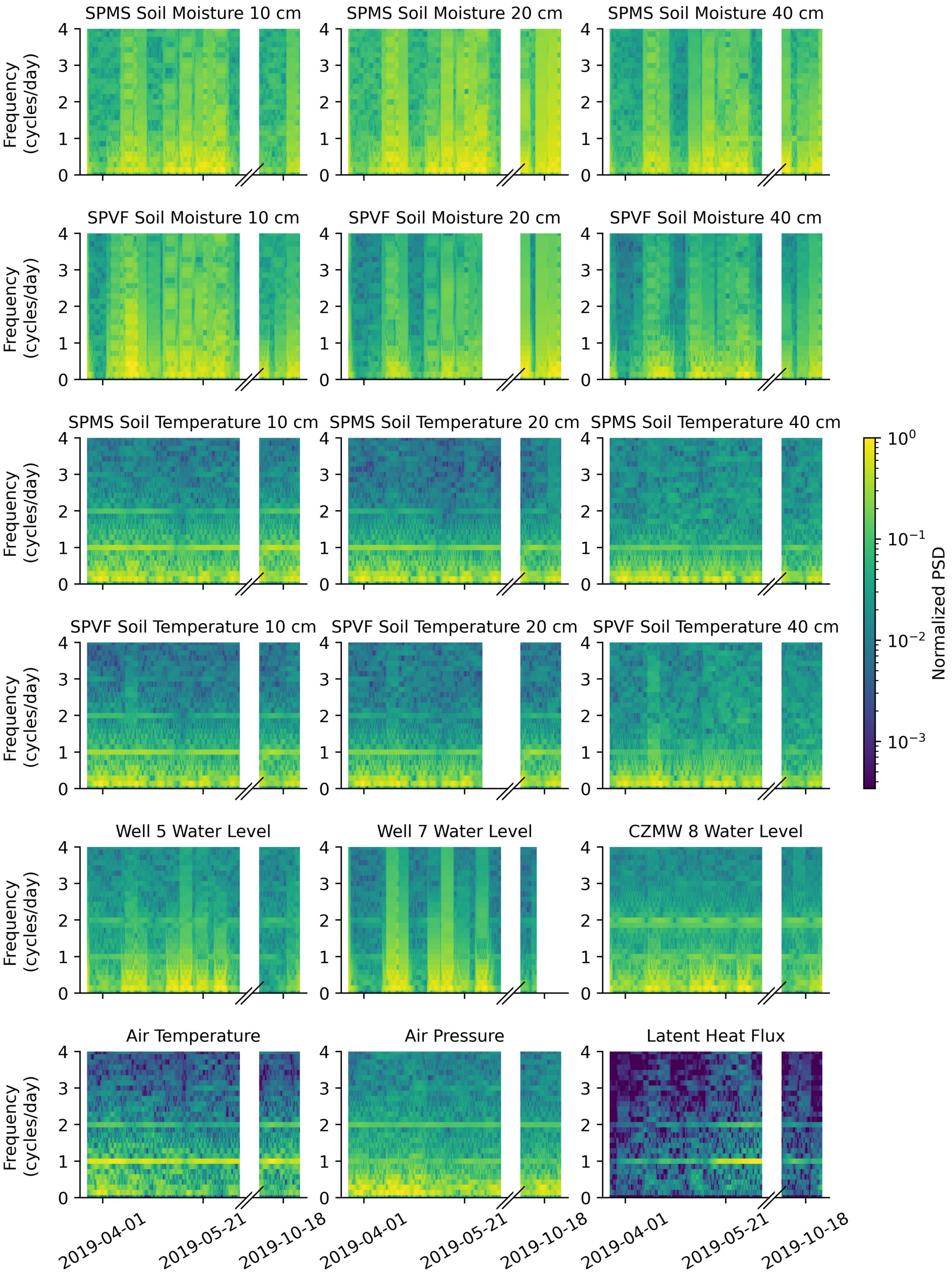
SPMS Soil Moisture 10 cm
SPMS Soil Moisture 20 cm
SPMS Soil Moisture 40 cm
SPVF Soil Moisture 10 cm
SPVF Soil Moisture 20 cm
SPVF Soil Moisture 40 cm
SPMS Soil Temperature 10 cm
SPMS Soil Temperature 20 cm
SPMS Soil Temperature 40 cm
SPVF Soil Temperature 10 cm
SPVF Soil Temperature 20 cm
SPVF Soil Temperature 40 cm
Well 5 Water Level
Well 7 Water Level
CZMW 8 Water Level
Air Temperature
Air Pressure
Latent Heat Flux
Frequency (cycles/day)
0
1
2
3
4
2019-04-01
2019-05-21
2019-10-18
Normalized PSD
10^0
10^{-1}
10^{-2}
10^{-3}

Figure7.

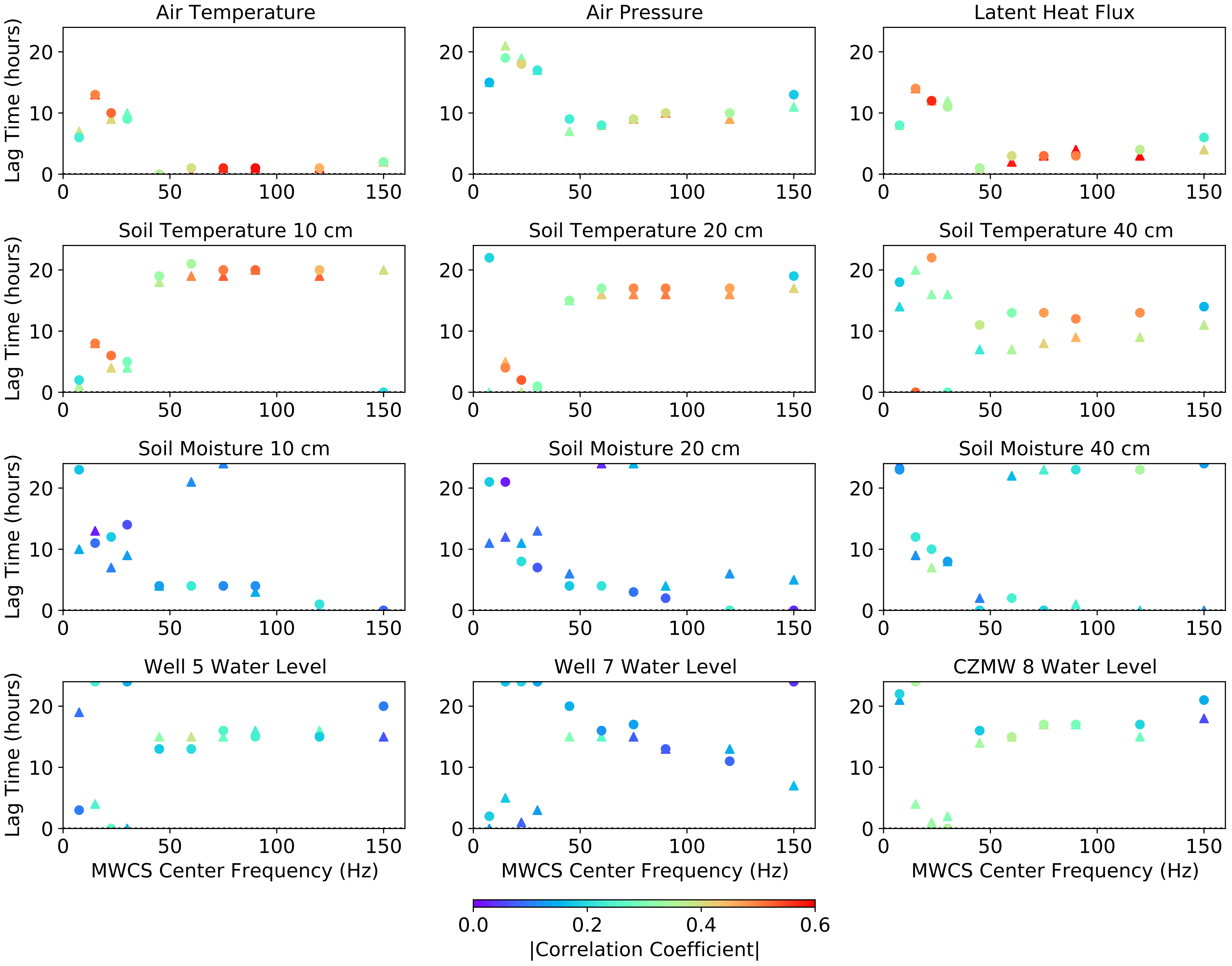
Air Temperature
Air Pressure
Latent Heat Flux
Soil Temperature 10 cm
Soil Temperature 20 cm
Soil Temperature 40 cm
Soil Moisture 10 cm
Soil Moisture 20 cm
Soil Moisture 40 cm
Well 5 Water Level
Well 7 Water Level
CZMW 8 Water Level
Lag Time (hours)
0
10
20
0
50
100
150
MWCS Center Frequency (Hz)
0.0
0.2
0.4
0.6
|Correlation Coefficient|

Figure8.

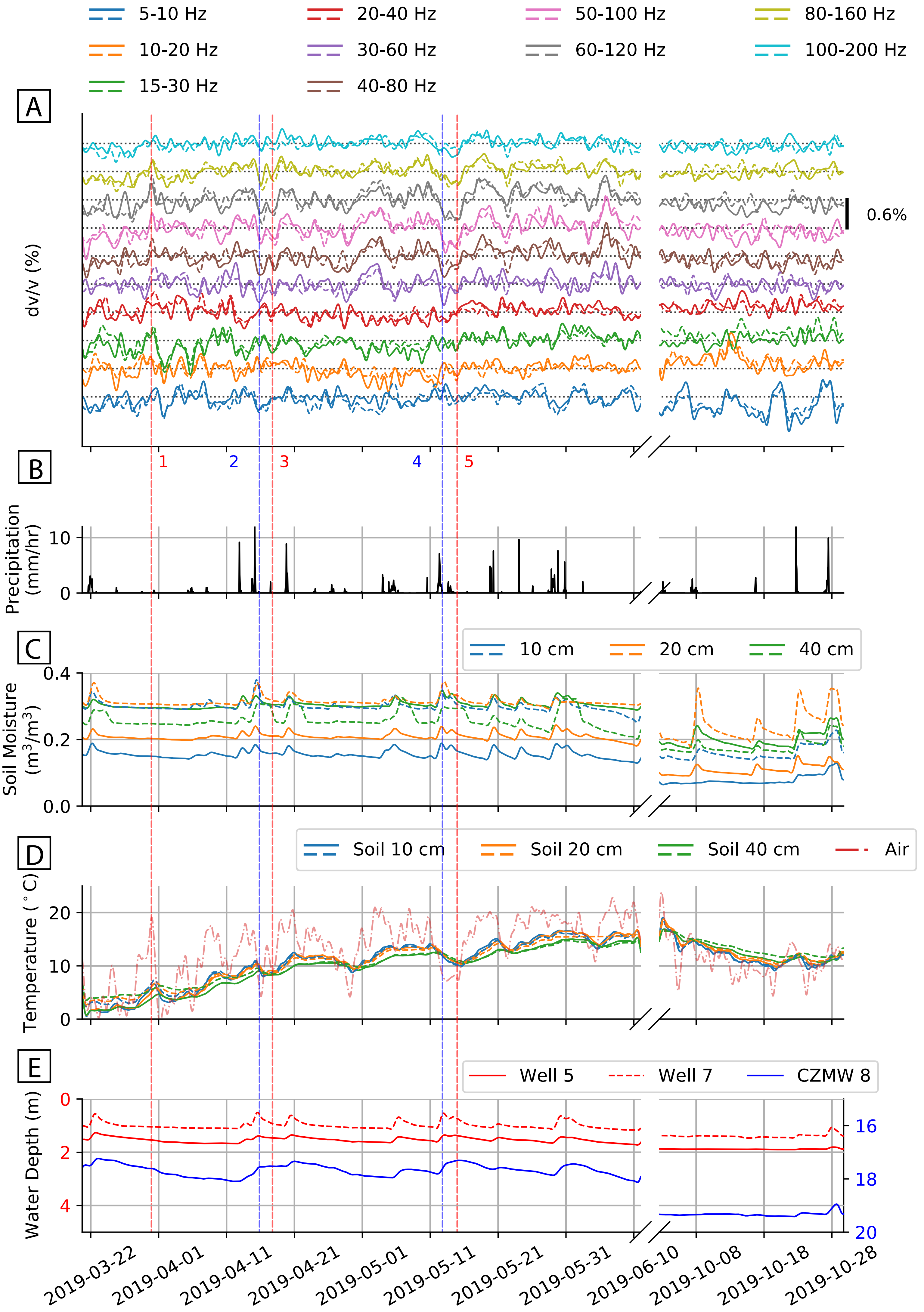
5-10 Hz
20-40 Hz
50-100 Hz
80-160 Hz
10-20 Hz
30-60 Hz
60-120 Hz
100-200 Hz
15-30 Hz
40-80 Hz
A
dv/v (%)
0.6%
1
2
3
4
5
B
Precipitation (mm/hr)
10
0
C
10 cm
20 cm
40 cm
Soil Moisture (m^3/m^3)
0.4
0.2
0.0
D
Soil 10 cm
Soil 20 cm
Soil 40 cm
Air
Temperature ($^\circ$C)
20
10
0
E
Well 5
Well 7
CZMW 8
Water Depth (m)
0
2
4
16
18
20
2019-03-22
2019-04-01
2019-04-11
2019-04-21
2019-05-01
2019-05-11
2019-05-21
2019-05-31
2019-06-10
2019-10-08
2019-10-18
2019-10-28

Figure9.

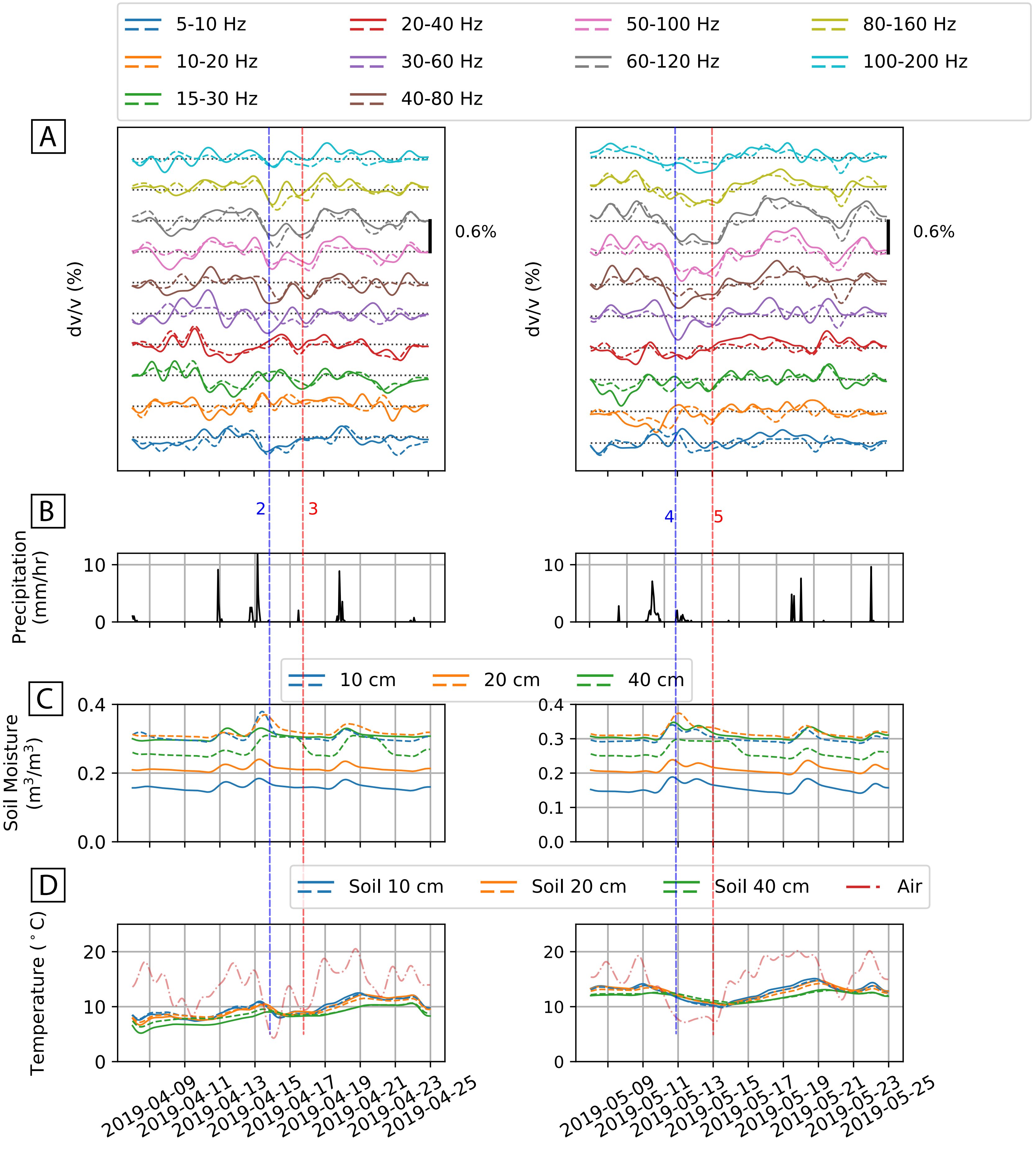
5-10 Hz
10-20 Hz
15-30 Hz
20-40 Hz
30-60 Hz
40-80 Hz
50-100 Hz
60-120 Hz
80-160 Hz
100-200 Hz
A
dv/v (%)
0.6%
dv/v (%)
0.6%
B
2
3
4
5
Precipitation (mm/hr)
10
0
C
10 cm
20 cm
40 cm
Soil Moisture (m^3/m^3)
0.4
0.2
0.0
0.4
0.3
0.2
0.1
0.0
D
Soil 10 cm
Soil 20 cm
Soil 40 cm
Air
Temperature ($^\circ$C)
20
10
0
2019-04-09
2019-04-11
2019-04-13
2019-04-15
2019-04-17
2019-04-19
2019-04-21
2019-04-23
2019-04-25
2019-05-09
2019-05-11
2019-05-13
2019-05-15
2019-05-17
2019-05-19
2019-05-21
2019-05-23
2019-05-25